Molecular solar thermal storage integration for domestic hot water co-heating: experimental discharge characterization and numerical

Journal of Energy Storage 178 (2026) 123498

Contents lists available at ScienceDirect

Journal of Energy Storage

journal homepage: www.elsevier.com/locate/est

Research papers

Molecular solar thermal storage integration for domestic hot water co-heating: experimental discharge characterization and numerical feasibility assessment

Ali Naman Karim [a,*], Giovana Fantin Do Amaral Silva [b], Zakariaa Refaa [c], Zhihang Wang [d], Jessica Orrego Hernandez [e], Liang Fei [g], Pär Johansson [a], Angela Sasic Kalagasidis [a], Kasper Moth-Poulsen [e,f,g,h,**]

[a] Department of Architecture and Civil Engineering, Division of Building Services Engineering, Chalmers University of Technology, SE-41296, Gothenburg, Sweden
[b] Bengt Dahlgren Göteborg AB, Krokslätts Fabriker 52, 431 37, Mölndal, Sweden
[c] Sever Pharma Solutions, P.O. Box 590, 201 25, Malmö, Sweden
[d] School of Engineering, College of Science and Engineering, University of Derby, Markeaton Street, Derby, DE22 3AW, United Kingdom
[e] Department of Chemistry and Chemical Engineering, Chalmers University of Technology, SE-41296, Gothenburg, Sweden
[f] The Institute of Materials Science of Barcelona, ICMAB-CSIC, Bellaterra, 08193, Barcelona, Spain
[g] Department of Chemical Engineering, Universitat Politecnica de Catalunya, EEBE, Eduard Maristany 10-14, 08019, Barcelona, Spain
[h] Catalan Institution for Research & Advanced Studies, ICREA, Passeig Lluis Companys 23, 08010, Barcelona, Spain

ARTICLE INFO

Keywords:
MOST
Norbornadiene-Quadricyclane
Molecular
Solar thermal energy
Thermal storage
water co-heating

ABSTRACT

Molecular solar thermal storage (MOST) systems represent an emerging closed-loop technology with energy storage densities up to 1.6 MJ/kg, more than double that of typical phase change materials. MOST systems store solar energy in the chemical bonds of photoswitchable molecules via photoisomerization, releasing heat on demand during molecular reversion. Despite extensive research, their potential for domestic hot water co-heating remains unexplored. This study investigates the potential integration of MOST systems into a conceptual laboratory-scale co-heating device by combining experimental discharge characterization with numerical thermal simulations. Laboratory experiments evaluated the discharge characteristics of a norbornadiene-quadricyclane MOST system, demonstrating thermal activation for the first time under varying activation temperatures and residence times. A numerical thermal simulation model was developed to assess the performance of two norbornadiene-quadricyclane systems designed for short- and long-term storage. Parametric studies analyzed the impact of molecular properties and device design parameters on discharge and water heating performance. Laboratory results demonstrated 95–100% back conversion of quadricyclane to norbornadiene at a molecular concentration of 1.3 mol/L (290.2 g/L) in toluene. Simulations indicated activation-normalized water-heating ratios of 43–86% for the long-term system and 106–204% for the short-term system, assuming perfect insulation and current molecular and device constraints, representing idealized upper-bound estimates. Among the MOST molecular properties evaluated, thermal enthalpy had the strongest sensitivity effect on discharge and water-heating performance. Additional gains were achieved through increased energy storage capacity, optimized molecule concentration, and adjusted device operational temperatures. Future research should prioritize molecular enhancements, catalytic strategies to accelerate back-conversion, and device design optimization to minimize heat losses and improve scalability.

Abbreviations: MOST, Molecular solar thermal storage; TES, Thermal energy storage; NBD-QC, Norbornadiene-quadricyclane derivatives; $t_{1/2}$, Half-life time; f1, Chemical shift; HEX, Heat exchanger.

* Corresponding author.
** Correspondence to: K. M.-Poulsen, Department of Chemistry and Chemical Engineering, Chalmers University of Technology, SE-41296, Gothenburg, Sweden.
E-mail addresses: ali.karim@chalmers.se (A.N. Karim), Kasper.moth-pulsen@chalmers.se (K. Moth-Poulsen).

https://doi.org/10.1016/j.est.2026.123498
Received 13 March 2026; Received in revised form 23 May 2026; Accepted 5 July 2026

1. Introduction

The energy sector accounts for over 75% of greenhouse gas emissions in the European Union (EU) [1]. In 2023, the EU increased its renewable energy target to a minimum of 42.5% by 2030, up from the 30% target set in 2018. Achieving this goal requires a significant transition from fossil fuels to renewable energy across all sectors, with the building sector playing a central role. Heating and cooling in buildings and industry constitute approximately 50% of the EU's total energy use. Yet, as of 2023, renewable energy sources provided less than 27% of the energy used for heating and cooling in buildings [2].

Solar energy is a key resource for low-carbon heat in buildings. However, its intermittency creates a temporal mismatch between energy supply and demand [3]. Thermal energy storage (TES) technologies are widely recognized as effective solutions to address this mismatch and facilitate peak shaving in domestic heating systems. Alternative approaches include electrochemical batteries, hydrogen storage, and carbon dioxide conversion [4,5]. Established TES technologies utilize sensible heat, latent heat, or thermochemical storage [3]. Compared with conventional sensible heat storage, latent TES, often incorporating phase change materials, and thermochemical TES typically offer higher energy density and associated space-saving benefits.

1.1. Molecular solar thermal storage

In addition to established TES technologies, molecular solar thermal storage (MOST) systems represent a novel and promising closed-loop approach [5]. MOST systems uniquely enable direct solar energy storage with extended storage durations at room temperature. This potential has attracted significant research interest in recent years [5–11]. MOST systems store solar energy in the chemical bonds of photoswitchable molecules. Upon exposure to solar irradiation, the parent molecule undergoes photoisomerization, converting into a high-energy isomer (charged state) [8], as depicted in Fig. 1. This metastable isomer can revert to its original state, releasing stored heat during the back-conversion (discharge) process. Discharge can be triggered thermally, catalytically, optically, or electrochemically [5]. MOST systems typically include dissolved solid molecules in a solvent for use in flow devices [5,7]. Compared to conventional TES technologies, MOST systems feature several advantages: (1) direct solar energy storage, (2) relatively high energy densities, (3) storage durations ranging from minutes to several years at room temperature, and (4) they operate in a closed cycle, making them emission-free during operation.

To identify the most effective MOST system, various photoswitchable molecules have been explored [7]. Prominent examples include norbornadiene [12], ruthenium [13], azobenzene [14], and dihydroazulene [15]. An ideal MOST system must meet several criteria [7]: (1) the parent molecule should absorb a broad range of the solar spectrum, (2) spectral overlap between the parent molecule and its photoisomer should be minimal, (3) the photoreaction should achieve a quantum yield (ratio of isomerization events to absorbed photons) of 100%, (4) the energy density should exceed 300 kJ/kg, (5) the photoisomer must remain kinetically stable for extended periods, and (6) the system should support multiple charge-discharge cycles with minimal degradation. Despite significant advancements, no single MOST system has met all these criteria, and the search for more efficient systems continues [5]. Among the candidates, the norbornadiene-quadricyclane (NBD-QC) system has gained considerable attention [5,7–9,11,16,17]. It stands out for its high energy storage density, reaching up to 1.6 MJ/kg [18], which is more than twice that of most phase change materials [19,20]. Furthermore, NBD-QC systems enable long-term storage of up to several decades [21–23]. However, challenges remain, including the system's primary absorption of ultraviolet-visible light and relatively low quantum yields for photoisomerization [5].

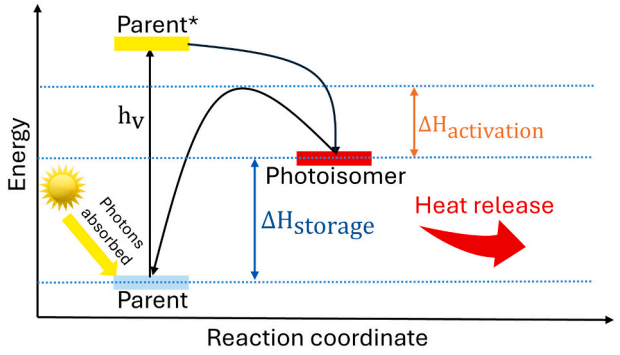

Fig. 1. Schematic representation of the closed cycle in a MOST system. h_v denotes the energy required to excite the parent molecule (charging). $\Delta H_{activation}$ represents the activation energy needed for back conversion from the high-energy photoisomer to the lower-energy parent molecule (discharging). The stored energy ($\Delta H_{storage}$) is released as heat on demand during this process.

In a study by Wang et al. [24], the efficiency of MOST systems for solar energy collection was assessed using parametric model calculations. Their findings indicated a maximum theoretical storage efficiency of 20.5% for an ideal MOST system, with the rest of the solar energy remaining unused. To address this limitation, several studies have explored hybrid technologies that integrate MOST systems to utilize more of the unused solar spectrum and enhance overall efficiency [5].

Dreos et al. [7] examined a small-scale hybrid solar water heating device that combined a fluidic chip containing a MOST system with a water heating unit. Experimental results showed that up to 1.1% of the incident solar energy could be stored in the MOST system, which utilized a maximum concentration of 0.1 mol/L dissolved in toluene. The hybrid device achieved a combined solar utilization efficiency of up to 80%. Fang et al. [17] theoretically investigated a hybrid photochemical-thermochemical system, where the MOST system provided photochemical storage while the thermochemical process captured the remaining solar spectrum. Unabsorbed photons from the MOST system were used to generate heat for methanol decomposition, resulting in a maximum average solar chemical efficiency of approximately 75%. In a related study, Fang et al. [16] evaluated a hybrid photochemical-photovoltaic-thermochemical system. The MOST system was utilized for photochemical storage, achieving a calculated maximum solar utilization efficiency of around 67%.

Wang et al. [11] developed a hybrid device combining a photovoltaic solar cell for electricity generation with a thin layer of a MOST system. The MOST layer was designed to store high-energy photons not captured by the cell while simultaneously cooling the cell. The study demonstrated that the MOST system could store up to 2.3% of solar energy, surpassing the previous record of 1.1% [7]. Additionally, the surface temperature of the photovoltaic cell was reduced by approximately 8 °C under solar irradiation, achieving a total solar utilization efficiency of around 15% [11]. In a separate study, Wang et al. [25] tested a proof-of-concept by integrating a MOST system film with a microfabricated thermoelectric generator. This setup aimed to convert the stored energy in the MOST system into electricity, even without solar radiation. With a MOST concentration of 0.78 mol/L and a solvent volume of less than 1 mL, the system achieved a power output of 1.3 W/m^3. These findings highlight the potential of MOST systems for efficient solar energy storage and conversion to electricity. Refaa et al. [9] investigated the thermo-optical performance of energy-saving windows featuring a thin, transparent film of a MOST system. The film stored solar energy during the day and released it as heat later. Simulations showed that the MOST film could efficiently act as an ultraviolet shield while storing up to 0.37 kWh/m^2.

Beyond these studies, research has explored integrating MOST systems with phase change materials [26–28]. These efforts aimed to introduce activation energy barriers for phase change material solidification, develop portable TES systems, and extend TES durations across

various temperature ranges. The reviewed literature primarily focuses on small-scale devices, many of which remain at the proof-of-concept stage. Over the past 40 years, no large-scale MOST devices have been developed [5], however, significant progress has been made in optimizing MOST systems. Current research therefore focuses on improving energy density, storage properties, and practical aspects like the achievable concentration of MOST systems in fluid solvents.

As noted earlier, domestic heating applications can play a vital role in reducing the environmental impact of the energy sector. Consequently, research into alternative TES solutions for domestic heating remains a priority. One promising but underexplored application of MOST systems is their potential for continuously heating fluids, such as water, in domestic heat generating systems. In addition, they could locally boost delivered temperatures in district heating networks, enabling lower supply temperatures and improving overall system efficiency.

Building on these potentials, this study investigates MOST systems as supplementary solutions for domestic water co-heating. It provides experimental evidence of thermally triggered discharge and evaluates the numerical feasibility of integrating MOST systems into a conceptual co-heating device. Given the current limitations in MOST molecule production and the absence of prior studies on this application, the research focuses on a small-scale setup in the laboratory. A conceptual design of the device is proposed, integrating MOST discharge with water co-heating. To assess feasibility, multiple realistic scenarios are simulated for two existing MOST systems designed for short-term and long-term TES applications. These scenarios reflect typical temperature profiles of domestic water co-heating systems and design parameters used in the laboratory environment. Parametric studies evaluate heat release during discharge, heat transfer to water, and resulting temperature profiles in the device. The results provide insights into optimizing design parameters and MOST molecule properties to enhance system efficiency and viability for hot water co-heating applications.

1.2. Overall methodology and layout

The study included both experimental and numerical approaches. Laboratory measurements focused on one of the two selected MOST systems to investigate and validate its discharge performance. Thermal activation was demonstrated for the first time in this context. Two concentrations of the MOST system were dissolved in the solvent and converted from the photoisomer back to the parent state. Temperature-dependent discharge characteristics were measured under controlled conditions. These measurements served as the basis for developing a numerical model that represents the thermal performance of a conceptual co-heating device. Parametric simulations analyzed the discharge characteristics of the MOST systems and the temperature development of both the MOST systems and water in the device across various scenarios. The simulations assessed the impact of device design parameters and MOST system properties on discharge and water heating efficiencies.

The paper is structured as follows: Section 2 details the two MOST systems investigated, and the experimental studies conducted. Section 3 introduces the conceptual design of the co-heating device, the numerical model, the defined scenarios and parametric studies. Section 4 presents the experimental and numerical results. Section 5 discusses the results, including the modelling assumptions and the MOST system performance relevant for the further device development. Finally, the appendices provide supporting experimental and numerical analyses, including replicate back-conversion measurements and additional analyses of practical factors affecting device performance, such as heat losses.

2. Materials and experimental studies

2.1. Materials

The two selected MOST systems, based on norbornadiene-quadricyclane (NBD-QC) derivatives (Fig. 2), represent short- and long-term TES durations while maintaining comparable properties (Table 1). The first system, NBD1-QC1, is designed for long-term applications, with an energy storage half-life ($t_{1/2}$) of approximately 28 days at 25 °C [29]. The half-life represents the time required for half of the photoisomer (QC) to revert to the parent molecule (NBD) at a given temperature. It is calculated using Eq. (1) and Eq. (2) [30–32]. The second system, NBD2-QC2, is optimized for short-term TES, with a much shorter half-life of around 5 h at 25° C [23]. Despite their differing half-life, both systems exhibit comparable energy storage densities of approximately 396 kJ/kg, enabling consistent performance comparisons across scenarios.

As noted in Section 1, MOST systems are dissolved in solvents. In this study, toluene was selected due to its low polarity, which improves solubility [33]. Previous measurements showed that MOST molecules in toluene experienced less than 0.14% degradation per cycle over 43 cycles [29].

$$t_{1/2} = \frac{\ln(2)}{k(T)} \tag{1}$$

$$k(T) = \frac{k_b \bullet T}{h_p} \bullet e^{\left(\frac{T \bullet \Delta S_{thermal} - \Delta H_{thermal}}{R \bullet T}\right)} \tag{2}$$

Where, $t_{1/2}$ (s) is the half-lite time, T (K) is the absolute temperature, k (T) (1/s) is the temperature-dependent back conversion rate, k_b (J/K) is the Boltzmann constant [$1.381 \bullet 10^{-23}$ J/K], h_p (J•s) is the Planck constant [$6.626 \cdot 10^{-34}$ J•s], and $\Delta H_{thermal}$ (kJ/mol) and $\Delta S_{thermal}$ (J/(mol•K)) are the thermal enthalpy and entropy changes, respectively. Finally, R (J/(mol•K)) is the universal gas constant [8.3145 J/(mol•K)].

2.2. Experimental studies

Laboratory measurements were conducted to investigate the discharge characteristics of the NBD1-QC1 MOST system, focusing on the thermally triggered back conversion of the photoisomer (QC) to the parent molecule (NBD). Key parameters such as activation temperatures, residence times, and their effects on back conversion rates (%) were evaluated and compared with the numerical model (Eqs. (1)–(2)) for validation. The experimental protocol is outlined in the following subsections.

2.2.1. Preparation of QC1 isomers

The parent NBD1 molecules were synthesized following the procedure outlined in [29]. Solutions of NBD1 in toluene-d_8 were prepared at concentrations of 1 mol/L (223.28 g/L) and 1.3 mol/L (290.2 g/L), nearing the highest concentration of 1.5 mol/L reported to date [29].

To evaluate the photoisomerization rate (%) and determine the maximum flow rate (mL/min) required for 100% conversion of NBD1 to QC1 at these concentrations, tests were conducted using a Vapourtec R4/R2+ flow chemistry reactor (Fig. 3). In these tests, solutions of NBD1 in toluene-d_8 (10 mL) were pumped through the photoreactor, illuminated by a 365 nm LED lamp (simulating solar irradiation), at room temperature. Flow rates were varied, starting from 0.33 mL/min. The photoisomerization rate was measured using proton nuclear magnetic resonance (^{1}H NMR) spectroscopy at 400 MHz.

Fig. 4 shows the ^{1}H NMR spectroscopy results, highlighting the chemical shifts (f1, ppm) for the parent NBD1 molecule and its photoisomerized QC1 solutions at concentrations of 1 mol/L and 1.3 mol/L. The spectra analysis, including downfield (higher ppm) and upfield

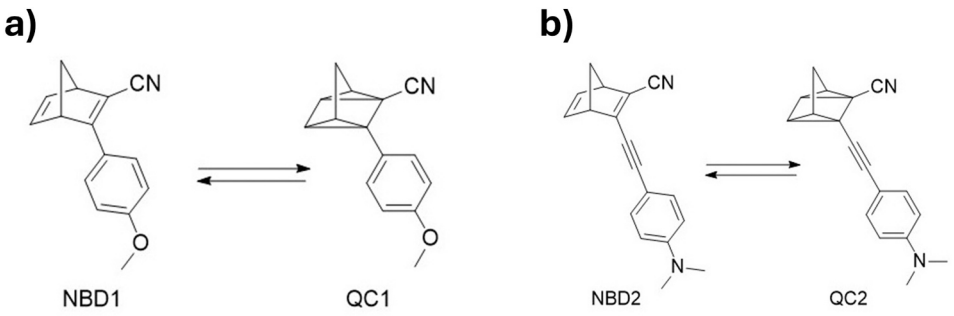

Fig. 2. Chemical structure of the two MOST derivatives: a) NBD1-QC1, b) NBD2-QC2.

Table 1
Relevant properties of the materials and the two MOST systems used in experimental and numerical simulation studies.

Property	NBD1-QC1[a, b, c]	NBD2-QC2[b,d]	Toluene[a, b,f]	Water[b,e]	Copper[b, e]
Thermal enthalpy, $\Delta H_{thermal}$ (kJ/mol)	103.8	92.5	–	–	–
Thermal entropy, $\Delta S_{thermal}$ (J/(mol•K))	−22	−19.1	–	–	–
Storage density, $\Delta H_{storage}$ (kJ/mol)	88.5	103	–	–	–
Storage density, $\Delta H_{storage}$ (kJ/kg)	396.4	395.6	–	–	–
Half-life time, $t_{1/2}$ (at 25 °C)	27.9 days	4.9 h	–	–	–
Molar mass, M (g/mol)	223.28	260.34	–	–	–
Specific heat capacity, c_p (kJ/(kg•K))	1.66[g]	1.66[g]	1.71	4.18	3.40
Density, ρ (kg/m^3)	985[g]	985[g]	866.5	1000	8960
Thermal conductivity, λ (W/(m•K))	–	–	0.13	0.6	395
Dynamic viscosity, μ (N•s/m^2)	–	–	$5.6•10^{-4}$	$8.9•10^{-4}$	–

[a]-Used in the experimental studies, [b]-Used in the simulation studies. Data collected from: [c]- [29], [d]- [23], [e]-[34], [f]- [35,36], [g]- [37].

(lower ppm) peaks, along with peak integration (reflecting the proportion of NBD1 converted to QC1), confirmed nearly 100% photoisomerization at both concentrations. The measurements also determined that the maximum flow rate for complete isomerization under the experimental conditions was 10 mL/min.

2.2.2. Back conversion of QC1 isomers to NBD1 parents

The prepared photo-converted MOST solutions were used for back conversion measurements. An automated back conversion experiment was conducted using a flow reactor (Vapourtec). The setup included a single flow stream containing a QC1 solution in toluene at a concentration of 1.3 mol/L (290.2 g/L), as shown in Fig. 5. A volume of 2 mL QC1 solution was pumped into a 5 mL reactor under varying temperatures, flow rates, and residence times. A 1-bar back pressure regulator maintained system pressurization. To address the slow back conversion rate at lower temperatures, elevated activation temperatures (90–110 °C) were selected based on the thermophysical properties of the NBD1-QC1 system ($\Delta H_{thermal}$ and $\Delta S_{thermal}$). The effect of residence time was examined at 105 °C, with residence times ranging from 5 to 25 min, corresponding to flow rates between 0.33 and 1.9 mL/min. The MOST solution was analyzed using ^{1}H NMR spectroscopy (400 MHz) to determine the back conversion rate (%) from QC1 to NBD1, evaluating the influence of temperature and residence time. To assess reproducibility, two additional replicate measurements were performed at 105 °C and 25 min residence time.

3. Numerical studies

3.1. Co-heat device using MOST systems

To assess the feasibility of MOST systems for water heating applications, a tailor-made co-heating device was conceptualized. As shown in Fig. 6, the device consists of two main components: (1) an activation unit and (2) a double-pipe heat exchanger (HEX). The activation unit initiates the discharge of the MOST system before it enters the HEX. Discharge can be triggered either thermally, by preheating the MOST system, or chemically, via a catalyst. The heat released during discharge increases the temperature of the MOST fluid to the desired level. Once the target temperature is achieved, the MOST fluid flows into the HEX. In this double-pipe HEX, the heated MOST fluid passes through the inner pipe, surrounded by an outer pipe carrying colder water. Heat is transferred from the warm MOST fluid to the inner pipe wall through convection. It then conducts through the pipe wall and is subsequently transferred to the water in the outer pipe through convection.

3.2. Numerical thermal simulations of the co-heating device

The numerical model was built using the explicit finite volume method in MATLAB R2023b to solve the heat and mass balance equations within the device. It simultaneously captures two key thermodynamic processes: the discharge of the MOST system, which starts in the activation component and results in a continuous temperature rise in the MOST solution, and the heat transfer between the two fluids in the heat exchanger. To streamline the simulations while maintaining focus on the primary thermal dynamics of the device, simplifying assumptions were made. The external surfaces exposed to the environment were treated as adiabatic, thereby excluding heat losses to the surroundings. Pressure was assumed to remain constant along the pipe, and the flow was considered laminar and free from irregularities or obstructions. Thermophysical properties were assumed constant, and heat conduction was considered only in the radial direction, while longitudinal conduction was neglected. The model also excluded any potential degradation of MOST molecules at elevated temperatures.

3.2.1. Activation component: discharge of the MOST system

In the numerical model, the activation component was represented as a cylindrical pipe with an inner radius r_1 (m), outer radius r_2 (m), and length L_{act} (m), as depicted in Fig. 7. The MOST system, with an initial concentration A_{00} (mol/m^3) of molecules dissolved in toluene, an initial temperature T_{00} (°C), and a flow velocity v_M (m/s), was pumped from a storage reservoir into the activation component (Fig. 6). The volumetric flow rate was assumed to be constant along the length of the component. Temporal and spatial discretization in the activation component were defined by dt (s) and dx (m), respectively.

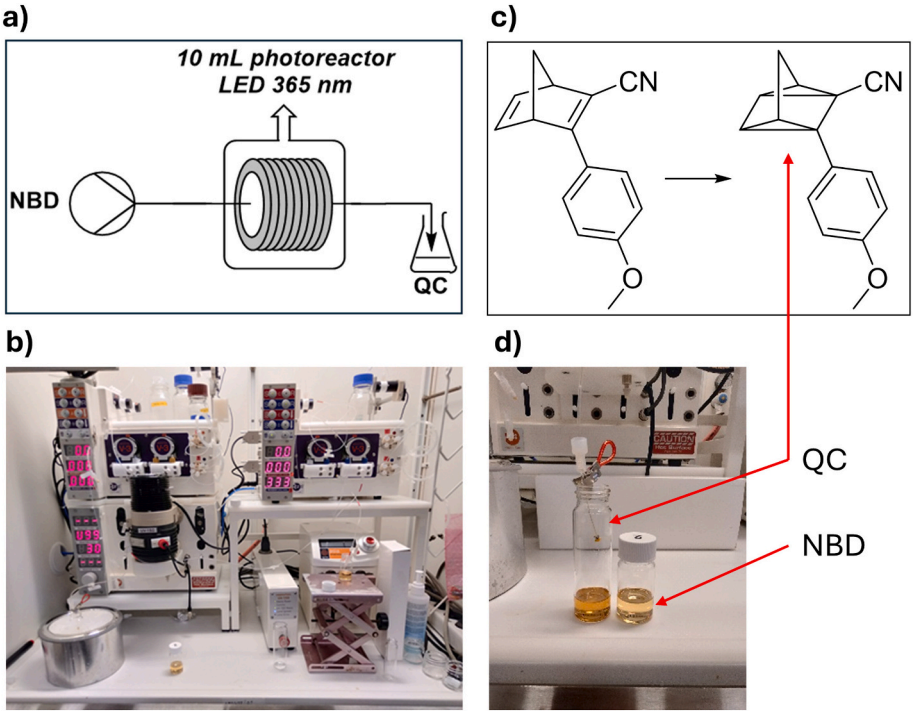

Fig. 3. a, b) Experimental setup, including the flow chemistry reactor used for the photoisomerization of NBD1 to QC1. c) Chemical structure of NBD1 (left) and QC1 (right). d) NBD1 dissolved in Toluene-d_8 (pale yellow, right bottle) and the QC1 solution (dark yellow, left bottle) after photoisomerization.

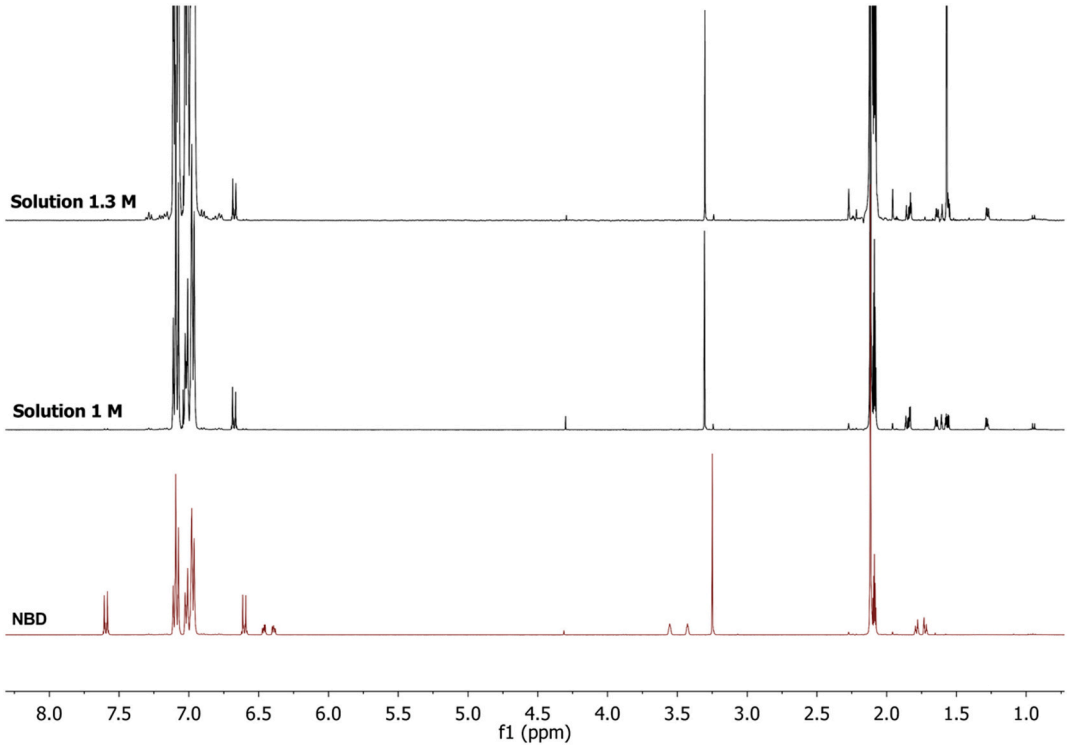

Fig. 4. ^{1}H NMR spectra (400 MHz, toluene-d_8) for NBD1 (red line) and QC1 (black lines) after photoisomerization at concentrations of 1 mol/L and 1.3 mol/L, showing nearly 100% conversion to QC1. The x-axis indicates the chemical shift (f1, ppm). (For interpretation of the references to colour in this figure legend, the reader is referred to the web version of this article.)

Upon entering the activation component, the MOST solution requires an external activation input to initiate or accelerate QC-to-NBD back-conversion. In the present model, this input is represented by a linearly distributed thermal source term, q_{act} (W/m^3), calculated using Eq. (3) and applied incrementally along the activation component. This source term should be interpreted as a modelling approximation of controlled thermal activation, rather than as a specific engineering design for heat supply.

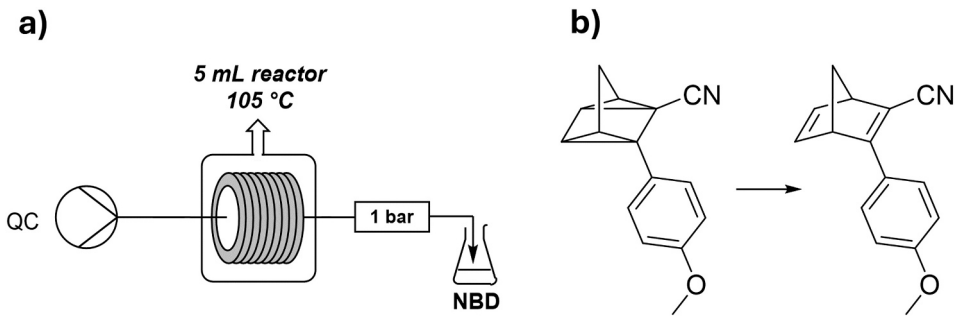

Fig. 5. a) Schematic of the experimental setup used for the back conversion of QC1 to NBD1. b) Chemical structures of QC1 (left) and NBD1 (right).

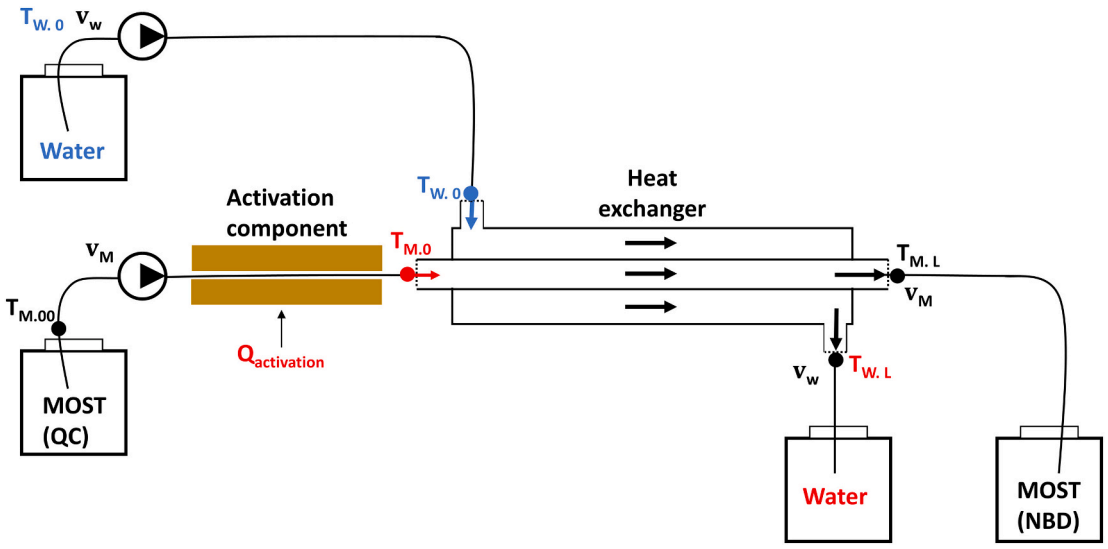

Fig. 6. Schematic of the conceptual co-heating device. The MOST solution, dissolved in a solvent, undergoes discharge in the activation component, triggered either thermally ($Q_{activation}$ (W)) or chemically using a catalyst. This process releases heat, raising the temperature of the system. Once the desired temperature is reached, the MOST system flows into the double-pipe heat exchanger, where colder water in the outer pipe is heated by the warmer MOST system in the inner pipe. T and v represent temperature (°C) and flow velocity (m/s), respectively. Subscripts M and w refer to the MOST system and water. Checkpoints labeled '00,' '0,' and 'L' indicate the position of the MOST solution before the activation component, at the start of the heat exchanger, and at the end of the heat exchanger length (L), respectively.

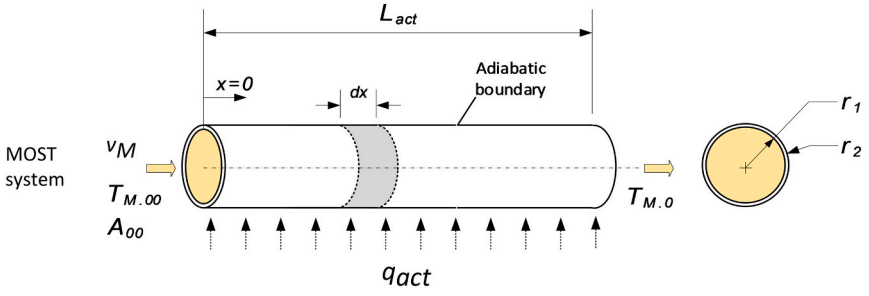

Fig. 7. Schematic of the activation component and the corresponding geometrical and physical parameters.

The activation source term was calculated from the theoretical thermal activation requirement and distributed over an assumed activation time, t_{act} (s). In the model, t_{act}, controls the rate of external heat supply and therefore affects the required activation length, L_{act}, for a given flow velocity and target outlet temperature. A larger t_{act} represents slower distributed heat input and results in a longer activation component. The temperature rise in the activation component is governed by the combined effect of external activation heat and chemical heat released during QC to NBD back-conversion, which can promote further conversion of remaining QC molecules. Consequently, part of the required temperature increase is supplied by the exothermic discharge reaction, reducing the external activation heat needed to reach the target outlet temperature compared with a case where chemical heat release is neglected.

$$q_{act}(x) = q_{act} = \Delta H_{thermal} \bullet \frac{A_{00}}{t_{act}} \tag{3}$$

Here, q_{act} is the modeled volumetric external heat input used for thermal activation, $\Delta H_{thermal}$ is the thermal activation enthalpy, A_{00} is the inlet QC concentration, and t_{act} is the assumed time over which the

activation input is distributed.

The heat balance for a control volume within the activation component is expressed using the governing equation in convective-diffusion form as follows:

$$\frac{\partial T_M}{\partial t} = \alpha_M \bullet \frac{\partial^2 T_M}{\partial x^2} - v_M \frac{\partial T_M}{\partial x} + \frac{q_{act} + q_{rel}(x)}{\rho_M \bullet c_{p.M}} \quad (4)$$

Here T (°C, K) represents temperature, t(s) is time, and x (m) is the spatial coordinate along the pipe. α (m^2/s) is thermal diffusivity, v (m/s) is flow velocity, ρ (kg/m^3) and c_p (J/(kg•K)) are density and specific heat capacity, respectively. The subscripts M refers to the MOST system. The Expressions for ρ_M and $c_{p.M}$ are provided in Eqs. (5) and (6), respectively. q_{rel} (W/m^3) is the heat released during discharge of the MOST system, which is calculated using Eqs. (7)–(9) in conjunction with Eq. (2). The subscript (s) refers to the solvent.

$$\rho_M = \rho_m \bullet \frac{V_m}{V_M} + \rho_s \bullet \left(1 - \frac{V_m}{V_M}\right) \quad (5)$$

$$c_{p.M} = \frac{m_m}{m_M} \bullet c_{p.m} + \left(1 - \frac{m_m}{m_M}\right) \bullet c_{p.s} \quad (6)$$

$$q_{rel}(t) = \Delta H_{storage} \bullet \frac{dA(t)}{dt} \quad (7)$$

$$A(t) = A_{00} \bullet e^{-k(T)\bullet t} \quad (8)$$

To express $q_{rel}(t)$ in terms of a spatial derivative $\frac{dA(t)}{dx}$ instead:

$$q_{rel}(x) = \Delta H_{storage} \bullet \left(\frac{dA(t)}{dt} \bullet \frac{dt}{dx}\right) = \Delta H_{storage} \bullet \left(v_M \bullet \frac{dA(t)}{dx}\right) \quad (9)$$

Here, $\Delta H_{storage}$ (J/mol) denotes the energy storage density of the MOST system (Table 1). A(t) (mol/m^3) represents the time-dependent concentration decay of the MOST molecules (QC) during discharge, described by a psuedo-first-order kinetic reaction equation [30,31,38]. A_{00} (mol/m^3) is the initial concentration of the MOST system at the start of the activation component. k(T) (s^{-1}) is the temperature-dependent conversion rate, presented in Eq. (2). The term $\frac{dA(t)}{dt}$ represents the temporal derivative of the concentration decay.

In the heat balance eq. (4) used in the numerical model, the diffusion term ($\alpha_M \bullet \frac{\partial^2 T_M}{\partial x^2}$) is negligible compared to the convective term ($v_M \frac{\partial T_M}{\partial x}$). This simplification is justified by the high Peclet numbers ($Pe >> 1$) resulting from the characteristics of the pipe and the MOST system [39], indicating that convective heat transport dominates over diffusion within the activation component. The Peclet number is defined as ($Pe_M = \frac{v_M \bullet L_c}{\alpha_M}$), where L_c (m) is the characteristic length. For the circular pipe in the activation component, L_c equals the hydraulic diameter, $2 \bullet r_1$. Under these conditions and the assumption of steady-state flow with a constant volumetric flow rate, the governing heat balance eq. (4) can be simplified and rewritten as Eq. (10):

$$v_M \frac{\partial T_M}{\partial x} = \frac{q_{act} + q_{rel}(x)}{\rho_M \bullet c_{p.M}} \quad (10)$$

As described earlier, activation heat is applied incrementally at each spatial step (dx) along the pipe. This heat is supplied continuously until the desired temperature is achieved, ensuring the total applied heat does not exceed the theoretical activation heat required for the complete discharge of the MOST system. Once the temperature in the activation component reaches the target level, driven by both the discharge of the MOST system and the applied activation heat, the system flows into the heat exchanger. At this stage, key parameters are determined, including the final temperature of the MOST system ($T_{M.0}$ (°C)), the remaining concentration of undischarged MOST molecules (A_0 (mol/m^3)), and the required length of the activation pipe (L_{act} (m)). If undischarged MOST molecules remain upon exiting the activation component, the model allows for continued discharge within the heat exchanger, provided the thermal conditions are suitable. The subsequent subsection details the processes occurring within the heat exchanger.

3.2.2. Heat exchanger: heating of water

The second section of the co-heating device is modeled as a concentric double-pipe heat exchanger (HEX). The heated MOST system flows through the inner pipe, which has an inner radius of r_1(m), identical to the activation component, see Fig. 8. This inner pipe is surrounded by an outer pipe with an inner radius of r_3(m), through which water circulates as the heat transfer fluid.

The HEX operates in a co-current flow configuration, with water supplied directly from a storage reservoir. Consequently, the water inlet temperature, $T_{W.0}$ (°C), is equal to the reservoir temperature. The MOST system's inlet temperature, $T_{M.0}$ (°C), corresponds to its outlet temperature from the activation component. Flow velocities for both the MOST system (v_M (m/s)) and water (v_W (m/s)) are assumed to remain constant along the entire length of the HEX (L_{hex} (m)). The exteriors of the pipes are considered adiabatic.

In the HEX, the water temperature is affected by two contributions from the MOST stream. The first is the sensible heat carried by the MOST solution as it enters the heat exchanger at an elevated temperature after the activation component. This sensible heat results from the externally supplied activation heat and, where back-conversion has already started, from chemical heat released in the activation component. The second contribution occurs when unconverted QC molecules remain after the activation component and continue to back-convert to NBD within the heat exchanger, releasing additional chemical heat. Heat is then transferred from the MOST solution to the water across the inner pipe wall separating the two fluids. For each spatial step, dx, the model calculates the heat released by ongoing MOST discharge, $q_{rel.i}$, and the heat transferred between the MOST solution and water, $q_{hex.i}$, independently. These heat fluxes are then combined using the superposition technique to update the temperature profiles of both fluids (Fig. 9). The updated temperatures serve as inputs for the next spatial step, and the procedure is repeated along the full HEX length to determine the outlet temperatures of the water, $T_{W.L}$, and the MOST solution, $T_{M.L}$.

In the first heat transfer process within the HEX, the heat balance equation at each spatial step is given by Eq. (11). This equation, along with the associated notation and criteria, follows the heat balance described in Eq. (10) for the activation component under steady-state conditions. The key distinction is that no external heat is applied to activate the MOST system within the HEX ($q_{act} = 0$).

$$v_M \frac{\partial T_M}{\partial x} = \frac{q_{rel}(x)}{\rho_M \bullet c_{p.M}} \quad (11)$$

The second heat transfer process, involving heat exchange between the MOST system and water, is modeled using the Number of Transfer Units (NTU) method [40], a standard approach in heat exchanger design. The NTU method evaluates the thermal performance of a heat exchanger using two dimensionless parameters. The first parameter, NTU, quantifies the heat exchanger's effectiveness in transferring heat between the hot and cold fluids, based on its configuration (e.g., counterflow or parallel flow). The second parameter, effectiveness (ε), represents the ratio of the actual heat transfer to the maximum possible heat transfer in an ideal heat exchanger. The mathematical formulations of the NTU method, as implemented in the numerical model, are provided in Eqs. (12)–(21).

$$NTU = \frac{U \bullet A_{pipe}}{C_{min}} \quad (12)$$

$$\epsilon = \frac{1 - e^{\left(-NTU \bullet \left(1 + \frac{C_{min}}{C_{max}}\right)\right)}}{1 + \frac{C_{min}}{C_{max}}} \quad (13)$$

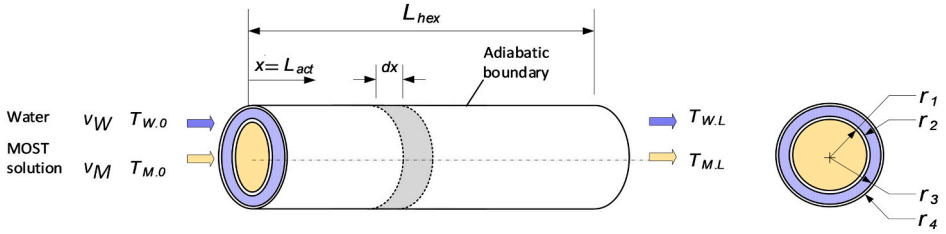

Fig. 8. Schematic of the heat exchanger and the corresponding geometrical and physical parameters.

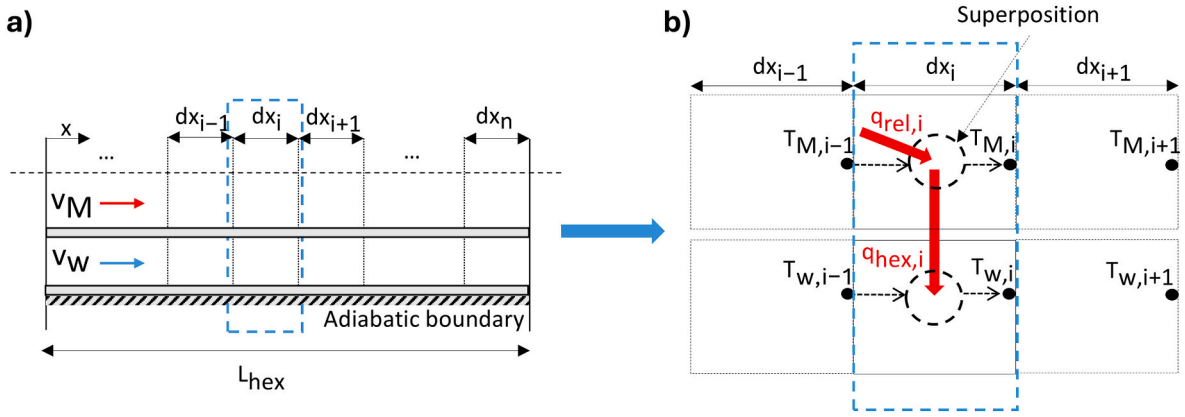

Fig. 9. Schematic (circular symmetry) of the heat exchanger (HEX) and the superposition method applied in the numerical model. a) The HEX is discretized into small spatial segments (dx) along its length ($0 < x < L_{hex}$), indexed by (i). b) For each segment (dx_i), the heat flux generated by the discharge of the MOST system ($q_{rel,i}$ (W/m^3)) and the heat transfer between the MOST system and water across the pipe wall ($q_{hex,i}$ (W/m^3)) are calculated independently. These heat fluxes are superposed to update the temperature profile, which is then used as the input for the next segment. This iterative process continues along the entire length of the HEX, determining the outlet temperatures $T_{M.L}$ (°C) and $T_{w.L}$ (°C) for the MOST system and water, respectively.

$$C_{min} = \min(C_M, C_w) \tag{14}$$

$$C_{max} = \max(C_M, C_w) \tag{15}$$

$$C_M = \dot{V}_M \bullet \rho_M \bullet c_{p.M} \tag{16}$$

$$C_w = \dot{V}_w \bullet \rho_w \bullet c_{p.w} \tag{17}$$

$$\dot{Q}_{max} = C_{min} \bullet (T_{M.0} - T_{w.0}) \tag{18}$$

$$Q_{hex} = \epsilon \bullet \dot{Q}_{max} \tag{19}$$

$$q_{hex.M}(x) = \frac{Q_{hex}}{V_M(x)} \tag{20}$$

$$q_{hex.w}(x) = \frac{Q_{hex}}{V_w(x)} \tag{21}$$

Where, U (W/(m^2•K)) is the overall heat transfer coefficient, incorporating the thermal conductivity of the inner wall of the annulus and the convection heat transfer coefficients of both fluids. A_{pipe} (m^2) represents the total heat transfer area, and C (W/K) denotes heat capacity rate. Q_{hex} (W) and q_{hex} (W/m^3) are the heat transfer flow and rate between the two fluids in the heat exchanger, respectively. V (m^3) represents volume. The subscripts min, max, M, and w, refer to minimum, maximum, MOST solution, and water, respectively.

The overall heat transfer coefficient, U (W/(m^2•K)), is expressed in Eq. (22), assuming no rust or scaling on the pipe surfaces. Here, h (W/(m^2•K)) represents the convective heat transfer coefficient of the fluid, A (m^2) is surface area of the pipe, and r (m) denotes the outer radius of the pipe. The subscripts i and o, refer to the inner and outer, respectively. The individual fluid heat transfer coefficients are determined using the Nusselt number, *Nu* (−), as shown in Eq. (23). For laminar flow, the Nusselt number is 3.657 [41]. λ_{hot} (W/(mK)) is the thermal conductivity of the hot fluid, in this case, the MOST system. L_c (m), is the characteristic length of the pipe.

$$U = \frac{1}{\frac{1}{h_i \bullet \left(\frac{A_i}{A_o}\right)} + \frac{1}{h_o} + \frac{r_o \bullet \ln\left(\frac{r_o}{r_i}\right)}{\lambda}} \tag{22}$$

$$h = \frac{Nu \bullet \lambda_{hot}}{L_c} \tag{23}$$

The heat balance equation in Eq. (24) is solved at each spatial step by superposing the two heat transfer processes. This calculation determines the temperature development of the MOST system and water in the heat exchanger.

$$v_M \frac{\partial T_M}{\partial x} - v_w \frac{\partial T_w}{\partial x} = \frac{q_{rel}(x) + q_{hex.M}(x)}{\rho_M \bullet c_{p.M}} - \frac{q_{hex.w}(x)}{\rho_w \bullet c_{p.w}} \tag{24}$$

3.2.3. *Parametric studies*

The developed numerical model was applied to simulate various scenarios, evaluating the thermal performance of the two MOST systems described in Section 2 within the activation component and heat exchanger of the co-heating device. These parametric studies focused on the conceptual feasibility and activation-normalized performance of the device for hot water co-heating applications. Key design parameters included inlet temperatures of the MOST systems and water, discharge activation rate, initial MOST molecule concentration, and selected molecular properties of the MOST system. Device configurations, such as pipe dimensions, wall material, and flow rates, were predefined based on laboratory constraints.

Two inlet water temperatures ($T_{w.0}$) were considered: 20 °C and 50 °C. The 20 °C setting represented ambient laboratory conditions and was included to evaluate the model response under a low inlet-temperature condition. The 50 °C case reflects a preheated domestic hot water condition and is directly aligned with the intended role of the proposed device as a co-heating or temperature-boosting unit. In this application, the MOST-based device would supplement an existing heat source by providing a final temperature lift, for example from 50 °C to 60 °C. This is relevant for Swedish domestic hot water systems, where approximately 50 °C is commonly required at tap-water outlets to reduce legionella risk, while higher temperatures, around 60 °C, are required for stored or stagnant hot water. Temperatures above approximately 65 °C are generally avoided to reduce the risk of scalding and scaling [42,43].

For the MOST systems, a storage reservoir temperature of 20 °C ($T_{M.00}$) was assumed. The temperature at the activation component outlet ($T_{M.0}$) ranged from 80 °C to 120 °C, based on experimental data ensuring full back conversion and sufficient heating to surpass the desired 60 °C water outlet temperature. Copper pipes were assumed due to their high thermal conductivity and availability. Liquid flow velocities were set at 0.007 m/s based on experiments demonstrating optimal back conversion rates (Section 2.2.1). Pipe dimensions, determined from a preliminary study (Appendix A), represented the minimum size required to achieve the target water heating from 50 °C to 60 °C. A spatial discretization of 0.7 mm was adopted, supported by a convergence analysis (Appendix A).

3.2.3.1. Simulated scenarios and performance indicators. To evaluate the influence of design parameters on the discharge characteristics of the two MOST systems and the device's water heating efficiency, six distinct scenarios (A-F) were defined and analyzed for each MOST system. In each scenario, a single parameter was varied while others remained constant, with performance assessed using the indicators described later in this section. The base-line case, Scenario 0, featured the first MOST system, NBD1-QC1, with discharge characteristics validated in the experimental studies. Scenarios 1-A to 1-F focused on NBD1-QC1, while Scenarios 2-A to 2-F explored the second MOST system, NBD2-QC2.

Scenario 0: base-line configuration

Table 2 summarizes the model characteristics for the baseline scenario (Scenario 0). The parameters established in Scenario 0 were maintained across the subsequent scenarios (A-F), except for the specific parameter under investigation. All simulations were conducted over a one-hour period. For the selected flow velocity, the total pipe length of the device ($L_{act} + L_{hex}$) was limited to approximately 25 m.

Scenario A: variable activation rate in the activation component

The activation rate of the MOST system discharge in the activation component is governed by the parameter t_{act} in the numerical model (Section 3.2.1). Together with the desired outlet temperature and selected flow velocity, t_{act} determines the length of the activation component (L_{act}). Scenario A examines t_{act} values of 300, 600, and 900 s (s).

Scenario B: variable inlet temperature of the MOST system in the heat exchanger

Scenario B investigates the effect of varying the MOST system inlet temperature in the heat exchanger ($T_{M.0}$), with values ranging from 80 °C to 120 °C.

Scenario C: variable inlet temperature of water in the heat exchanger

In scenario C, the water inlet temperature ($T_{w.0}$) in the heat exchanger varies between 20 °C and 50 °C.

Scenario D: variable concentration of MOST molecules

To assess the effect of MOST molecule concentration, Scenario D tests concentrations of 1 mol/L, 1.3 mol/L, and 2.6 mol/L. While concentrations up to 1.3 mol/L have been experimentally validated, 2.6 mol/L represents a theoretical case for future reference.

Scenario E: variable thermal energy storage capacity

Scenario E explores adjustments to the thermal energy storage capacity ($\Delta H_{storage}$, kJ/kg) of the MOST systems by factors of 0.5, 1.5, and 2. This aims to assess its impact on the performance of the MOST systems and the activation-normalized device performance, and guide future optimization of MOST systems.

Scenario F: variable thermal enthalpy

Scenario F examines the effect of reduced thermal enthalpy ($\Delta H_{thermal}$ (kJ/mol)), a key factor in accelerating back conversion. Adjustments by factors of 0.9, 0.7, and 0.5 are considered. This scenario is intended as an exploratory sensitivity analysis of activation-barrier effects, including the potential influence of catalyst-assisted discharge.

Table 2
Design characteristics of the device used in the base-line scenario investigated in the numerical studies.

Design choice	Designed value	Design choice	Designed value
r_1	3.5 mm	$T_{M.00}$	20°C
r_2	4.5 mm	$T_{M.0}$	105°C
r_3	5.5 mm	$T_{w.0}$	50°C
r_4	6.5 mm	v_M	0.007 m/s
Pipe wall material	Copper	v_W	0.007 m/s
A_{00}	1.3 mol/L	t_{act}	300 s
MOST system	NBD1-QC1	Activation type	Thermal

3.2.3.2. Performance indicators. To evaluate the effects of the design parameters studied on MOST discharge and water-heating performance, the following performance indicators (PIs) are defined:

Discharge rate of the MOST system: β (%)

The discharge rate β(x) represents the proportion of discharged MOST molecules at a given position (x) along the activation component or heat exchanger (Eq. (25)). It is calculated based on the concentration of discharged MOST molecules, A(x) (mol/L), relative to the initial concentration, A_{00} (mol/L), at the start of the activation component. Specific discharge rates are denoted as β_{act} (or $\beta(L_{act})$) for the end of the activation component and β_{device} (or $\beta(L_{act} + L_{hex})$) for the end of the heat exchanger.

$$\beta = 100 \bullet \frac{(A_{00} - A(x))}{A_{00}}, x \in [0, L_{act} + L_{hex}] \quad (25)$$

Activation-normalized discharge ratio of the MOST system in the Activation component: $R_{M.act}$ (%)

The PI $R_{M.act}$ (%) represents the ratio of the heat released by the discharge of the MOST system to the heat applied to activate the discharge in the activation component (Eq. (26)).

$$R_{M.act} = 100 \bullet \frac{Q_{M.rel}}{Q_{act}} = 100 \bullet \frac{\sum_{x=0}^{x=L_{act}} q_{rel}(x) \bullet V_M}{\sum_{x=0}^{x=L_{act}} q_{act}(x) \bullet V_M} \quad (26)$$

Activation-normalized total discharge ratio of the MOST System in the co-heating device: $R_{M.device}$ (%)

The PI $R_{M.act}$ (%) represents the total heat released by the MOST system at the end of the heat exchanger relative to the activation heat applied in the activation component (Eq. (27)).

$$R_{M.device} = 100 \bullet \frac{Q_{M.rel.total}}{Q_{act}} = 100 \bullet \frac{\sum_{x=0}^{x=L_{act}+L_{hex}} q_{rel}(x) \bullet V_M}{\sum_{x=0}^{x=L_{act}} q_{act}(x) \bullet V_M} \quad (27)$$

Activation-normalized water-heating ratio of the co-heating device: R_w (%)

The water heating ratio, R_W, represents the thermal power associated with co-heating water from its inlet temperature, $T_{w.0}$, to a specified higher temperature, normalized by the external activation heat supplied in the activation component. $R_{W.60}$ specifies the ratio for heating water

from $T_{w.0}$ to the targeted temperature of 60 °C (Eq. (28)), while $R_{W.device}$ specifies the ratio for heating water from $T_{w.}0$, to the actual outlet temperature at the end of the heat exchanger $T_{w.L}$ (Eq. (29)). Here, $\dot{V}_w$ (m^3/s) represents the volumetric flow rate of water.

$$R_{W.60} = 100 \bullet \frac{Q_{.w.outlet}(T_w = 60^{\circ}C)}{Q_{act}} = 100 \bullet \frac{\dot{V}_w \bullet \rho_w \bullet c_{p.w} \bullet (60 - T_{w.0})}{\sum_{x=0}^{x=L_{act}} q_{act}(x) \bullet V_M} \tag{28}$$

$$R_{W.device} = 100 \bullet \frac{Q_{.w.outlet.tot}}{Q_{act}} = 100 \bullet \frac{\dot{V}_w \bullet \rho_w \bullet c_{p.w} \bullet (T_{w.L} - T_{w.0})}{\sum_{x=0}^{x=L_{act}} q_{act}(x) \bullet V_M} \tag{29}$$

The PIs normalized by Q_{act} describe the useful heat output relative to the external heat supplied to initiate or accelerate back-conversion. They should therefore not be interpreted as complete thermodynamic or solar-to-heat efficiencies. The heat released during discharge originates from chemical energy previously stored in the QC isomer during the charging step. Since the present model focuses on the discharge and co-heating process, the solar charging step is outside the defined system boundary. Consequently, the activation-normalized indicators may exceed 100% when the released stored chemical energy and the resulting heat transferred to water exceeds the supplied activation heat.

4. Results

4.1. Experimental results

Figs. 10 and 11 present the laboratory measurements of the back conversion rate of the photoisomerized QC1 solution to its parent NBD1 molecule, highlighting the influence of temperature and residence time. Fig. 10 shows that near-complete back conversion (95–100%) was achieved within the selected temperature range of 90–110 °C. At 90 °C, the conversion rate was approximately 95% after 95 min, while at 110 °C, full conversion (100%) was attained within 15 min.

Fig. 11a illustrates the effect of residence time on back conversion at a constant temperature of 105 °C, with a calculated half-life of 5 min. As expected, longer residence times corresponded to higher conversion rates, increasing from 58% at 5 min (matching the calculated half-life) to 97% at 25 min. In Fig. 11b, theoretical predictions from the decay model (Eqs. (1)–(2)) are compared with experimental data. The model generally underestimated the back conversion rate by about 15% at a 5-minute residence time. However, at 25 min, the model prediction (97%) aligned with the experimental result. The replicate measurements at 105°C and 25 min further confirmed reproducible near-complete back-conversion, with conversion rates ranging from 97% to 98% (Appendix D, Fig. D1). These findings confirm that a residence time (25 min) of approximately five times the half-life (5 min) is sufficient to achieve near-complete back conversion (95–100%).

4.2. Numerical simulation results

To enhance the readability, the results of the parametric study are presented as follows: Fig. 12 illustrates the baseline scenario (Scenario 0) using the NBD1-QC1 MOST system, along with comparative results for the NBD2-QC2 system. A summary of all scenarios and their respective design parameters, aligned with the performance indicators (PIs), is shown in Figs. 13 and 14 and explained in this section. Detailed outcomes for each scenario (1-A to 1-F for NBD1-QC1 and 2-A to 2-F for NBD2-QC2) are included in Appendix B (Figs. B1 to B12) and follow the same structure as Fig. 12. The results presented in this section are based on the adiabatic main model and should therefore be interpreted as idealized upper-bound reference values for comparing the relative influence of the parameters studied.

In the base-line scenario, the required pipe length of the activation component (L_{act}) to reach an outlet temperature of 105 °C was approximately 1.9 m for NBD1-QC1 and 1.2 m for NBD2-QC2 (Fig. 12). This difference reflects the distinct half-life of the two systems: 28 days at 25 °C for NBD1-QC1 and 5 h at 25 °C for NBD2-QC2. For NBD1-QC1, 7% of the molecules were discharged in the activation component (β_{act}), resulting in an activation-normalized discharge heat ratio ($R_{M.act}$) of 6%. Conversely, NBD2-QC2 discharged 46% of its molecules (β_{act}), with $R_{M.act}$ reaching 90%. Full discharge was achieved almost immediately upon entering the heat exchanger (Fig. 12c).

In the heat exchanger, NBD1-QC1 heated water to 60 °C after 0.17 m and reached a maximum outlet temperature of 73 °C (Fig. 12 b). By this point, the total discharge rate (β_{device}) was 31% (Fig. 12 c). For NBD2-QC2, water reached 60 °C after 0.09 m, with a maximum temperature of 82 °C at 1.6 m. The activation-normalized total discharge heat ratio ($R_{M.device}$) was 30% for NBD1-QC1 and 195% for NBD2-QC2. The activation-normalized water-heating ratio to 60 °C ($R_{W.60}$) was 28% for NBD1-QC1 and 50% for NBD2-QC2. When considering the maximum attainable water temperature, the activation-normalized device water-

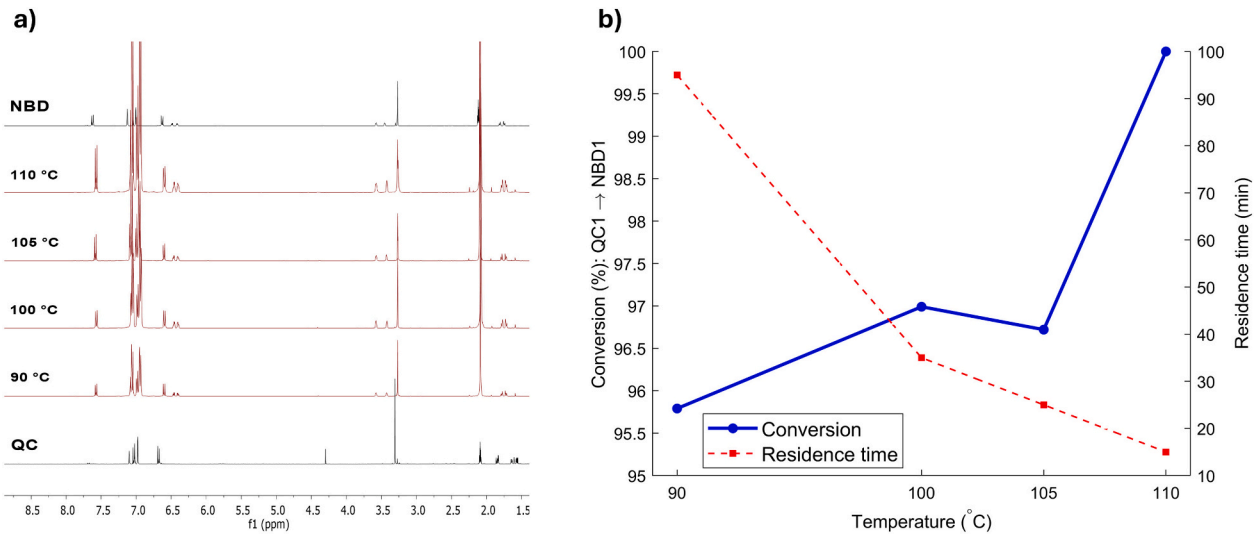

Fig. 10. a) ^{1}H NMR spectra (400 MHz, toluene-d_8) for QC1 (black line) and NBD1 (1.3 mol/L) solutions (red lines) after photoisomerization at temperatures between 90 and 110 °C. b) Measured back conversion rates and residence times corresponding to the spectra shown in a). (For interpretation of the references to colour in this figure legend, the reader is referred to the web version of this article.)

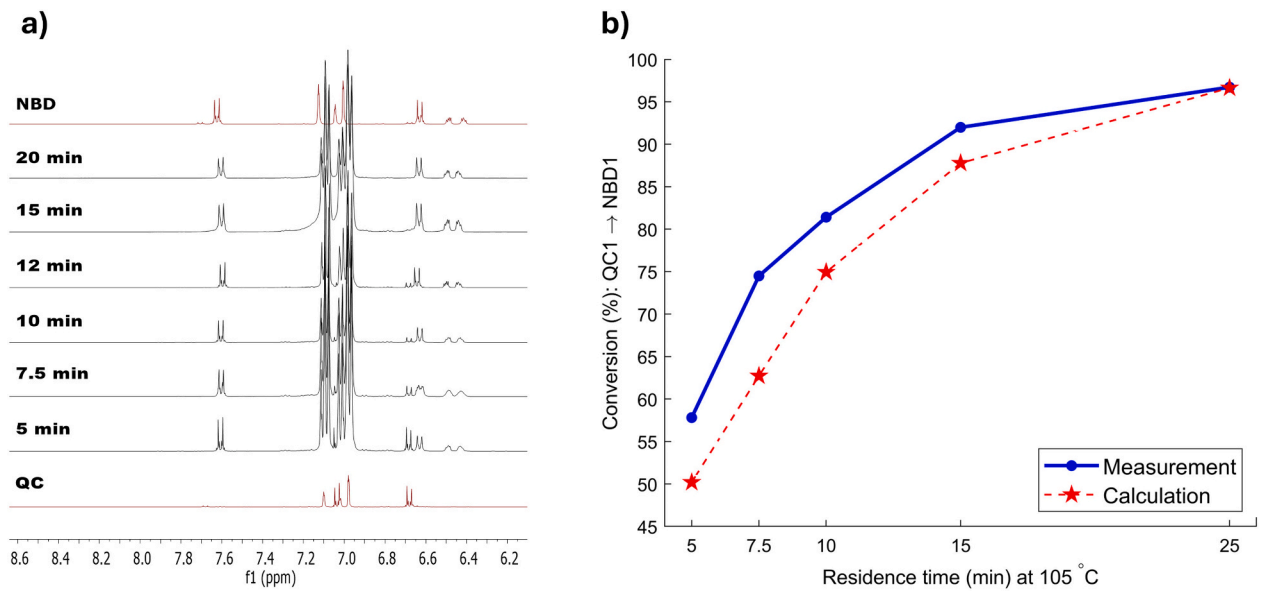

Fig. 11. a) ^{1}H NMR spectra (400 MHz, toluene-d_8) for QC1 and NBD1 (1.3 mol/L) solutions after residence times of 5–25 min at 105 °C. b) Measured and calculated back conversion rates as a function of residence times.

heating ratio ($R_{W.device}$) increased to 64% and 158%, respectively (Fig. 12 d).

The parametric study results, summarized in Figs. 13 and 14, show how variations in design parameters, operational conditions, and molecular properties affect MOST discharge and activation-normalized water-heating performance. The upper heat maps (Fig. 13a, Fig. 14a) compare scenarios focused on design and operational parameters (1-A to 1-D and 2-A to 2-D). The lower heat maps (13b, 14b) illustrate scenarios that explore potential molecular optimizations, representing theoretical cases (1-E, 1-F, and 2-E, 2-F).

4.2.1. Scenario 1-A and 2-A: t_{act}

Prolonging the activation time (t_{act}) from 300 s to 900 s improved the activation-normalized discharge and water-heating ratios for both MOST systems (Fig. 13a, and Figs. B1 and B2). For NBD1-QC1, increasing t_{act} raised the activation-normalized discharge ratio in the activation component , $R_{M.act}$, from 6% to 15% (127% increase) and the activation-normalized total discharge ratio ($R_{M.device}$) from 30% to 34% (14% increase). For NBD2-QC2, which already had a high base-line efficiency, its $R_{M.act}$ increased from 90% to 146% (62% increase), and $R_{M.device}$ rose from 195% to 254% (30% increase). Extending t_{act} also enhanced the discharge rate at the end of the activation component (β_{act}). For NBD1-QC1, β_{act} doubled from 7% to 14%, while for NBD2-QC2 it increased from 46% to 58%. These gains required lengthening the activation component from 1.9 m to 5.3 m for NBD1-QC1 and from 1.2 m to 2.8 m for NBD2-QC2. While β_{device} remained nearly unchanged for NBD1-QC1 (31–33%), NBD2-QC2 consistently achieved full discharge, regardless of t_{act}. Longer activation times also modestly improved the activation-normalized water-heating ratios. For NBD1-QC1, $R_{W.60}$ increased from 28% to 30%, while $R_{W.device}$ remained around 64%. For NBD2-QC2, $R_{W.60}$ rose from 50% to 65%, and $R_{W.device}$ increased from 158% to 185%. However, the extended activation time slightly reduced peak water temperatures: $T_{W.L}$ dropped by about 2 °C for NBD1-QC1 and 3 °C for NBD2-QC2. Thus, extending t_{act} resulted in greater discharged energy and activation-normalized water-heating ratios but reduced peak water temperatures. For NBD2-QC2, which inherently discharges more efficiently, the relative benefits of longer activation periods were less significant compared to NBD1-QC1.

4.2.2. Scenario 1-B and 2-B: $T_{M.0}$

Adjusting the MOST inlet temperature before the heat exchanger ($T_{M.0}$) notably influenced discharge and water heating performance (Figs. B3 and B4). For NBD1-QC1, lowering $T_{M.0}$ from 105 °C to 80 °C reduced the activation-normalized discharge ratio in the activation component ($R_{M.act}$) from 6% to 1% and activation-normalized total discharge heat ratio ($R_{M.device}$) from 30% to 13%. Conversely, increasing $T_{M.0}$ to 120 °C improved $R_{M.act}$ to 15% (133% above baseline) and $R_{M.device}$ to 52% (75% above baseline). The discharge rate in the activation component (β_{act}) increased from 7% to 17% (133% above baseline), and overall discharge (β_{device}) rose from 31% to 59% (91% above baseline). This greater energy release enhanced $R_{W.device}$ from 43% to 81% and raised the outlet water temperature ($T_{W.L}$) from 61 °C to 81 °C. However, $R_{W.60}$ decreased from 38% to 26%. For NBD2-QC2, which exhibited higher baseline activation-normalized ratios, $T_{M.0}$ adjustments had a smaller impact. Raising $T_{M.0}$ to 120 °C increased β_{act} from 46% to 63% and $R_{M.act}$ from 90% to 123%. Meanwhile, $R_{M.device}$ slightly decreased from 195% to 194%. Similarly, $R_{W.60}$ dropped from 53% to 49%, and $R_{W.device}$ from 163% to 157%. Despite these reductions, $T_{W.L}$ increased slightly from 81 °C to 82 °C. The results indicate that increasing $T_{M.0}$ improved discharge development for NBD1-QC1 and increased its final water-heating output, but reduced the activation-normalized ratio for heating water to 60 °C. For NBD2-QC2, higher $T_{M.0}$ mainly improved discharge in the activation component, while the total activation-normalized ratios changed only slightly or decreased marginally.

4.2.3. Scenario 1-C and 2-C: $T_{W.0}$

For NBD1-QC1, lowering $T_{W.0}$ from the baseline scenario of 50 °C to 20 °C or 35 °C prevented reaching the 60 °C outlet target (Fig. B5). Conversely, when $T_{W.0}$ was 65 °C, the water was already above the target temperature, making $R_{W.60}$ irrelevant. Regarding the activation-normalized device water-heating ratio, $R_{W.device}$, both reducing and increasing $T_{W.0}$ beyond the base-line enhanced the ratio, although with different effects on the outlet water temperature. Lowering $T_{W.0}$ to 20 °C increased $R_{W.device}$ to 75% (19% above base-line), though $T_{W.L}$ dropped from 73 °C to 47 °C. Raising $T_{W.0}$ to 65 °C pushed $R_{W.device}$ to 86% (35% above base-line) and increased $T_{W.L}$ from 73 °C to 95 °C. Changes in $T_{W.0}$ did not affect the activation component directly, but higher water temperatures in the heat exchanger facilitated additional back-conversion of the MOST solution. Raising $T_{W.0}$ to 65 °C increased β_{device} to 85% (172% above base-line) and $R_{M.device}$ to 86% (35% above baseline). For NBD2-QC2, varying $T_{W.0}$ had minimal impact on MOST

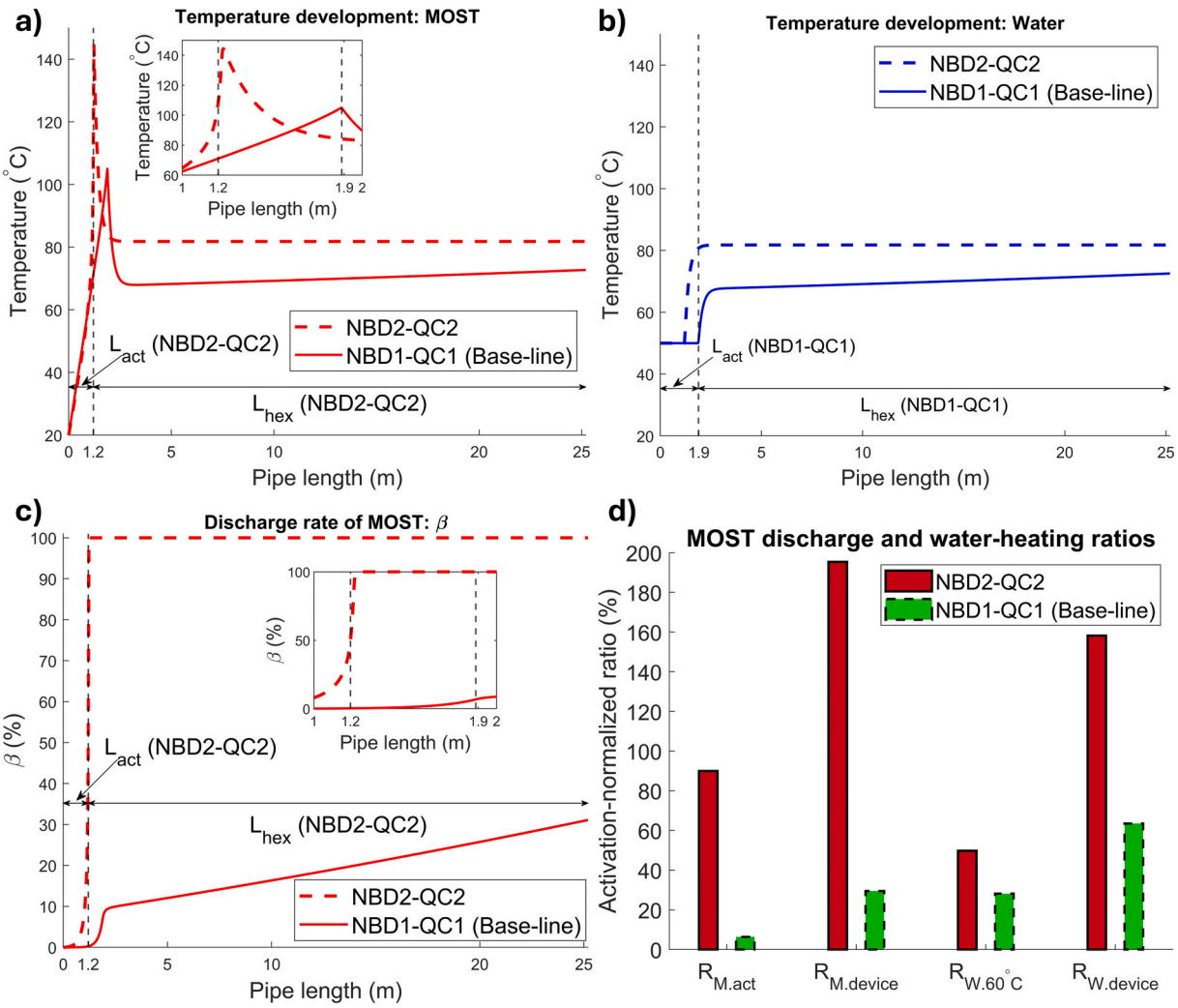

Fig. 12. Simulation results for the base-line scenario (Table 2) using the NBD1-QC1 MOST system, with comparable analyses for the NBD2-QC2 MOST system. The plots illustrate the temperature profile of a) the MOST systems and b) water, c) the discharge rate, and d) the activation-normalized MOST discharge and water-heating ratios.

discharge performance (Fig. B6). However, lowering $T_{W.0}$ improved the activation-normalized water-heating ratios while reducing the outlet temperature. Reducing $T_{W.0}$ to 20 °C increased $R_{W.60}$ to 199% (300% above base-line), although $T_{W.L}$ dropped from 82 °C to 61 °C. Similarly, $R_{W.device}$ increased to 204% (29% above base-line). Conversely, increasing $T_{W.0}$ to 65 °C lowered $R_{W.device}$ to 135% (15% below base-line) while raising $T_{W.L}$ from 82 °C to 92 °C. For NBD1-QC1, setting $T_{W.0}$ too low hindered achieving 60 °C, whereas NBD2-QC2 showed stronger temperature-boosting performance at lower inlet water temperatures due to its shorter half-life and faster discharge performance.

4.2.4. Scenario 1-D and 2-D: A_{00}

For NBD1-QC1, reducing the initial molecular concentration, A_{00}, from the base-line of 1.3 mol/L to 1.0 mol/L and 0.8 mol/L significantly improved the activation-stage discharge performance. $R_{M.act}$ increased from 6% to 24% and 54%, respectively, while the discharge rate (β_{act}) rose from 7% to 28% and 63%. These improvements required extending the activation component (L_{act}), which increased from 1.9 m in the base-line to 14 m at 0.8 mol/L (Fig. B7). Conversely, increasing A_{00} to 2.6 mol/L had limited impact on activation performance. β_{act} dropped to 3% (49% below base-line), and $R_{M.act}$ improved only slightly (1% above base-line). However, L_{act} decreased to 1.0 m compared to 1.9 m at base-line. In terms of activation-normalized total discharge ratio ($R_{M.device}$), both decreasing and increasing A_{00} outperformed the base-line, with higher concentrations yielding the most significant gains. At 2.6 mol/L, $R_{M.device}$ reached 108% (264% above base-line), while at 0.8 mol/L, it achieved 58% (95% above base-line). The activation-normalized water-heating ratios showed mixed results. Lowering A_{00} to 0.8 mol/L increased $R_{W.60}$ to 41% (46% above base-line), whereas raising A_{00} to 2.6 mol/L left $R_{W.60}$ nearly unchanged at 28% (1% below base-line). The device-level water-heating ratio ($R_{W.device}$) rose to 72% (13% above base-line) at 0.8 mol/L and to 116% (82% above base-line) at 2.6 mol/L. The final water outlet temperature ($T_{W.L}$) decreased by up to 7% when A_{00} was reduced but increased to 92 °C (26% above base-line) at 2.6 mol/L.

For NBD2-QC2, variations in A_{00} had less pronounced effects on activation performance (Fig. B8). A common trend emerged: increasing A_{00} improved most PIs except β_{act}, which decreased, and $R_{W.60}$, which remained nearly unchanged. Lowering A_{00} from 1.3 to 0.8 mol/L reduced $R_{M.act}$ by 3% (to 84%) but increased β_{act} by 55% (to 71%). Conversely, raising A_{00} to 2.6 mol/L boosted $R_{M.act}$ by 4% (to 93%) and decreased β_{act} by 48% (to 24%). In the heat exchanger, the MOST system temperature rose sharply with higher A_{00}, reaching approximately 235 °C at 2.6 mol/L. This elevated the final water outlet temperature ($T_{W.L}$) to 109 °C (33% above base-line). The activation-normalized total discharge ratio ($R_{M.device}$) increased to 390% (100% above base-line) at 2.6 mol/L. Meanwhile, $R_{W.60}$ remained steady near 50%, regardless of A_{00} variations. However, $R_{W.device}$ rose to 291% (84% above base-line) at

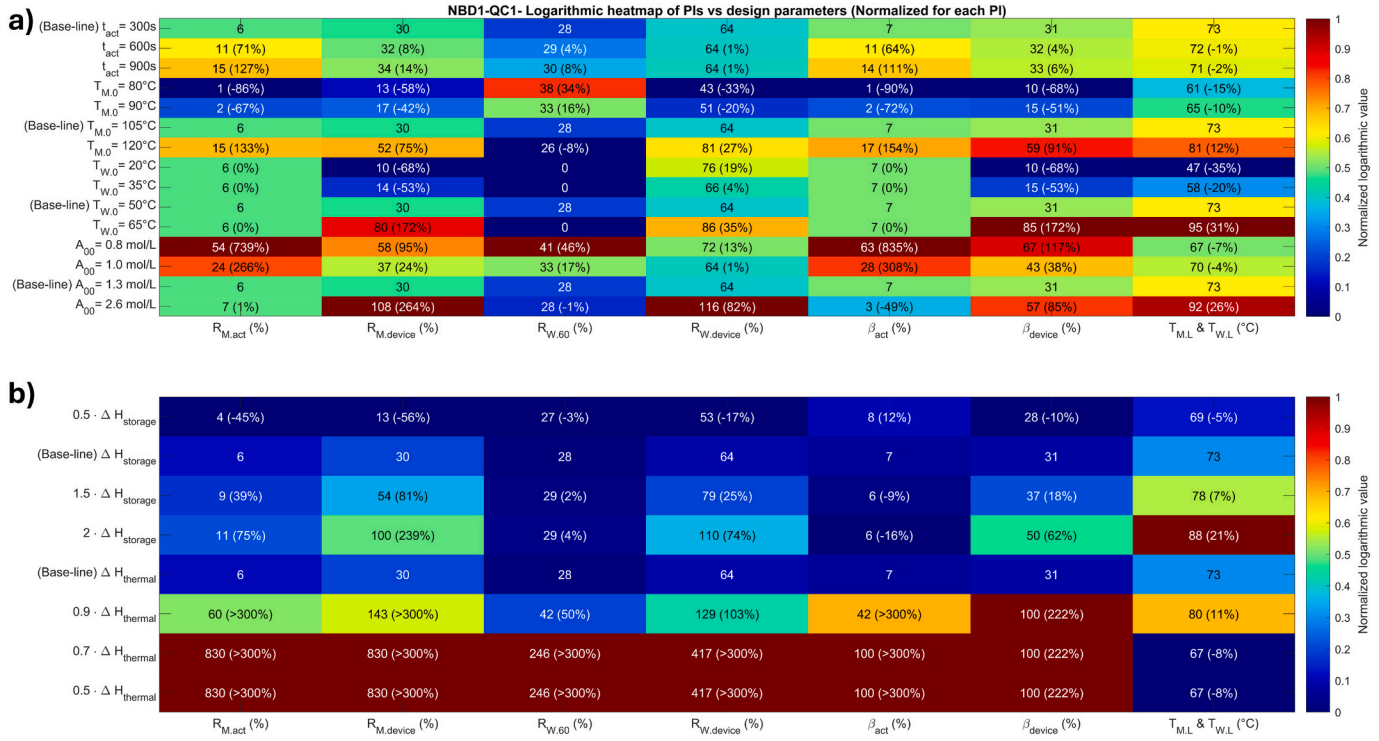

Fig. 13. Heat maps illustrating the impact of the studied design and operational parameters on the activation-normalized performance indicators for the NBD1-QC1 system under the adiabatic model assumption The heatmaps use a logarithmic scale normalized independently for each PI (columns) to highlight relative variations across each design parameter (rows). Rows marked as (Base-line) denote the reference cases within each parameter category (scenario). The colour scale represents normalized logarithmic values, with darker red indicating higher normalized impacts and blue indicating lower impacts. Numeric values printed in each cell correspond to the actual values of the PI. For rows other than the base-line, values in parentheses show the percentage change relative to the base-line of that parameter category. a) Device design parameters. b) Molecular design parameters. (For interpretation of the references to colour in this figure legend, the reader is referred to the web version of this article.)

2.6 mol/L and dropped to 106% (33% below base-line) at 0.8 mol/L.

These simulation results showed that, for NBD1-QC1, lower concentrations (A_{00}) improved activation-stage discharge performance but required longer activation lengths. Meanwhile, higher concentrations enhanced device-level activation-normalized discharge and water-heating ratios and increased the water outlet temperature. NBD2-QC2, with inherently higher discharge capabilities, showed less variation in performance but achieved greater device-level ratios at higher concentrations. However, these gains were accompanied by very high predicted MOST-system temperatures, highlighting a key challenge for practical implementation.

4.2.5. *Scenario 1-E and 2-E:* $\Delta H_{storage}$

In Scenario E, increasing the thermal energy storage capacity ($\Delta H_{storage}$) improved most PIs for both MOST systems, except for the discharge rate (β_{act}), see Figs. B9 and B10. For NBD1-QC1, raising $\Delta H_{storage}$ by a factor of 1.5 increased $R_{M.act}$ to 9% (39% above base-line) and $R_{M.device}$ to 54% (81% above base-line). The activation-normalized water-heating ratios also improved: $R_{W.60}$ increased to 29% (2% above base-line), and $R_{W.device}$ rose to 79% (25% above base-line). Doubling $\Delta H_{storage}$ pushed $R_{W.device}$ to 110% (74% above base-line).

For NBD2-QC2, raising $\Delta H_{storage}$ by 1.5 improved $R_{M.act}$ to 109% (21% above base-line), $R_{M.device}$ to 324% (66% above base-line), $R_{W.60}$ to 55% (11% above base-line), and $R_{W.device}$ to 243% (53% above base-line). Doubling $\Delta H_{storage}$ further enhanced $R_{W.device}$to 336% (112% above base-line).

4.2.6. *Scenario 1-F and 2-F:* $\Delta H_{thermal}$

In Scenario F, the effect of reducing thermal enthalpy ($\Delta H_{thermal}$) was analyzed as an exploratory sensitivity case representing a lower apparent activation barrier, for example through catalyst-assisted discharge or molecular design. The results showed that reducing $\Delta H_{thermal}$ significantly increased the activation-normalized discharge and water-heating ratios (Figs. B11 and B12). For NBD1-QC1, a 10% reduction in $\Delta H_{thermal}$ (0.9× base-line) increased the activation-normalized discharge heat ratio in the activation component ($R_{M.act}$) from 6% to 60% (828% improvement) and the activation-normalized total discharge heat ratio ($R_{M.act}$) from 30% to 143% (382% above base-line). The activation-normalized water-heating ratios also improved: $R_{W.60}$ rose from 28% to 42% (50% gain), and $R_{M.device}$ increased from 64% to 129% (103% above base-line). For NBD2-QC2, the same 10% reduction in $\Delta H_{thermal}$ boosted $R_{M.act}$ to 548% (509% above base-line) and $R_{M.device}$ to 643% (229% above base-line). The activation-normalized water-heating ratios, $R_{W.60}$ and $R_{W.device}$, increased to 164% (229% above base-line) and 362% (129% above base-line), respectively. Further reductions in $\Delta H_{thermal}$ (to 0.7× and 0.5× base-line) led to complete discharge (β_{act}: 100%) and $R_{W.60}$ and $R_{W.device}$ reaching 10^2–10^5%. These results indicate that $\Delta H_{thermal}$ had the strongest sensitivity effect among the parameters varied individually in the model, highlighting activation-barrier control as an important direction for future MOST development in co-heating applications.

5. Discussion

5.1. *Experimental studies*

As outlined in the introduction, research on optimizing MOST molecules is ongoing, with continuous development of new compounds. In this study, two NBD-QC molecules with distinct half-lives were selected to represent short-term and long-term storage capacities while maintaining comparable storage densities to ensure consistent performance

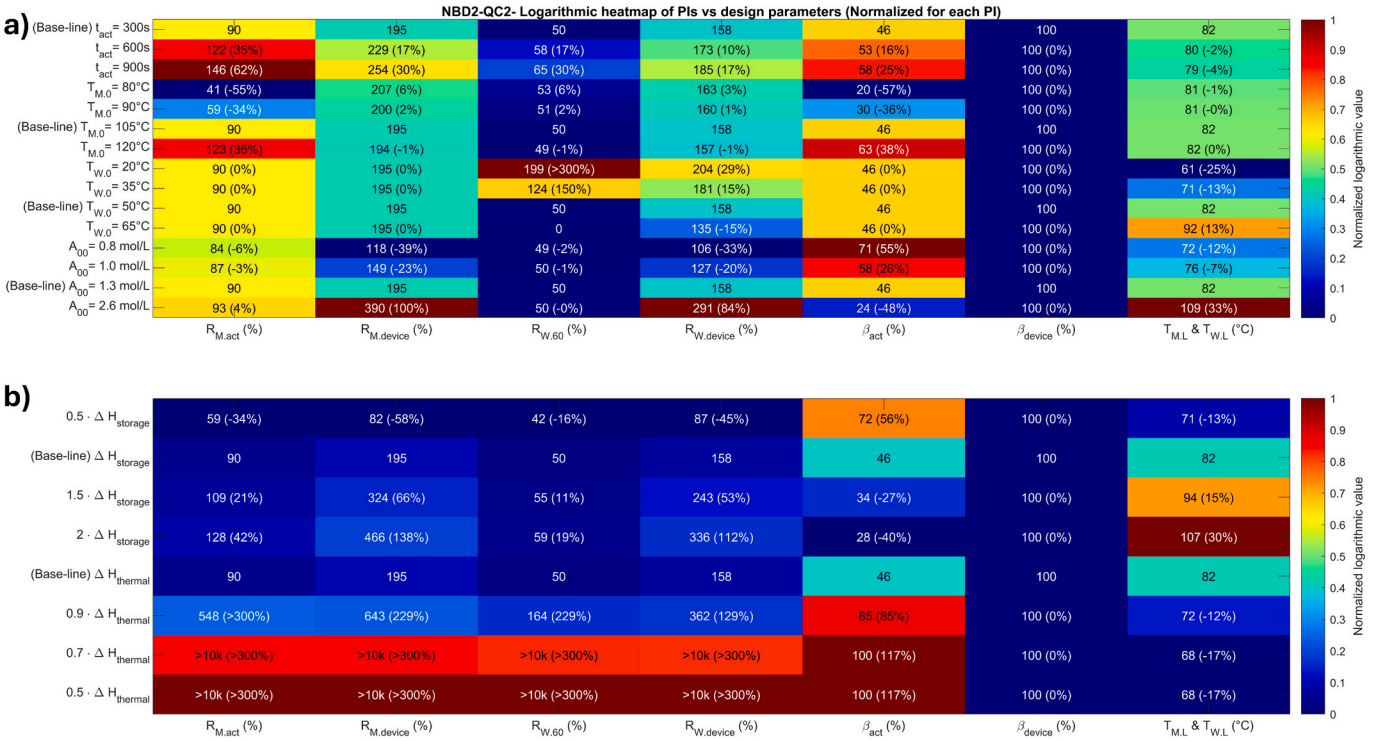

Fig. 14. Heat maps illustrating the impact of the studied design and operational parameters on the activation-normalized performance indicators for the NBD2-QC2 system under the adiabatic model assumption. The heatmaps use a logarithmic scale normalized independently for each PI (columns) to highlight relative variations across each design parameter (rows). Rows marked as (Base-line) denote the reference cases within each parameter category (scenario). The colour scale represents normalized logarithmic values, with darker red indicating higher normalized impacts and blue indicating lower impacts. Numeric values printed in each cell correspond to the actual values of the PI. For rows other than the base-line, values in parentheses show the percentage change relative to the base-line of that parameter category. a) Device design parameters. b) Molecular design parameters. (For interpretation of the references to colour in this figure legend, the reader is referred to the web version of this article.)

comparisons. While different MOST molecules could yield different quantitative outcomes, the primary aim was to investigate how different discharge characteristics may influence the feasibility of MOST-based water co-heating. The thermal behavior observed in the controlled laboratory setup provides trends that can be scaled up and used to guide the design of MOST-integrated heating devices. Together, these results outline the key factors that should be improved in future work to enable practical, real-world applications.

Laboratory measurements verified the discharge characteristics of NBD1-QC1 molecules dissolved in toluene-d_8. The preparation of QC1 isomers and their back-conversion to NBD1 followed established procedures [29]. A notable advancement was the demonstration of thermal back conversion for the first time and for relatively high concentrations (1 mol/L and 1.3 mol/L), nearing the previously reported maximum of 1.5 mol/L [29]. Under the tested conditions, near-complete back-conversion was achieved, supporting the feasibility of thermal discharge at these concentrations. Replicate measurements at 105 °C and 25 min confirmed reproducible near-complete back-conversion (97–98%). Future experimental work should expand replication to additional temperatures, residence times, and concentrations to further quantify uncertainty across the full experimental matrix.

The experimental work focused on NBD1-QC1, which was available at sufficient quantity and concentration for the laboratory discharge tests. NBD2-QC2 was included only in the numerical study as a literature-based short-term storage reference system, enabling comparison of how different storage half-lives and discharge kinetics influence device performance within the same modelling framework. Further experiments under relevant concentration, temperature, flow, and residence-time conditions are needed to validate the predicted performance of NBD2-QC2 in the co-heating configuration.

5.2. Numerical studies

Validation of the mathematical decay model against experimental data confirmed its capability to predict the discharge rate of MOST molecules with sufficient accuracy, although it consistently underestimated conversion rates. This conservative bias was most pronounced at shorter residence times, with a deviation of up to 15% at 5 min, decreasing to near zero at 25 min. This suggests that the numerical model provides a conservative estimate of discharge under the tested conditions.

The co-heating device and numerical model were intentionally simplified to focus on the primary thermal interactions between MOST discharge and water heating. This allowed the effects of molecular properties and device parameters to be isolated, but also means that the main parametric results should be interpreted as idealized upper-bound estimates rather than directly achievable practical device performance. This is particularly relevant for the adiabatic boundary condition, since heat losses reduce the temperature available for water heating and may affect the required activation and heat-exchanger lengths. Nevertheless, adiabatic or near-adiabatic conditions remain a useful reference for MOST heat-release analysis, as previous experimental work has shown that high macroscopic heat release can be achieved in well-designed flow systems [29]. The heat-loss case study in Appendix C confirms this sensitivity: negligible external convective losses reproduced the adiabatic baseline closely, whereas increased convective heat transfer caused clear performance degradation. However, the magnitude of these losses depends strongly on the selected technical design and pipe arrangement. For example, compact multi-pass configurations or adjacent high-temperature pipe sections could reduce the effective temperature difference to the surroundings compared with the conservative straight-pipe configuration used in Appendix C. Thus, the activation-

normalized water-heating ratios reported in the main results should be viewed as upper-bound reference values for comparing parameter effects, while Appendix C illustrates the importance of non-adiabatic boundary conditions for future device design.

The long activation lengths predicted in some scenarios indicate a design challenge for future practical device geometries. For example, the 14 m activation length obtained for NBD1-QC1 at 0.8 mol/L reflects the low concentration and slow discharge development under that specific set of assumptions. This suggests that the assumed distributed activation approach is not well suited for this case in a straight-pipe configuration, and that more compact activation configurations should be evaluated. The distributed heat-input representation should therefore be regarded as a modelling approximation for sensitivity analysis, rather than as a validated physical activation design. Therefore, t_{act} should be interpreted as a model parameter controlling activation intensity. Such straight-pipe activation lengths may not be suitable for compact domestic installation without further design development. Practical implementation should therefore evaluate more compact activation configurations, such as coiled or multi-pass heated channels, jacketed or electrically heated reactor sections, compact insulated reactor chambers, fixed-temperature heated reactors, or catalyst-assisted activation units. These approaches could increase residence time and heat-transfer area while reducing the physical footprint and insulation length.

The model assumptions related to heat transfer and material stability should also be considered when interpreting the results. Constant thermophysical properties and a fixed laminar-flow Nusselt number were used to provide a consistent basis for comparing the influence of MOST discharge, operating temperature, concentration, and molecular parameters. For future device-level design, the model can be refined by including temperature- and composition-dependent properties of the MOST solution and water, particularly in cases with large temperature changes or continued back-conversion within the heat exchanger. Such refinements may affect the predicted heat-transfer performance, pressure drop, and outlet temperatures. Experimental validation of heat-transfer coefficients under relevant operating conditions would further support practical design development. The model also excludes molecular and solvent degradation at elevated temperatures, which should be addressed in future experimental studies, especially for scenarios outside the experimentally validated concentration and temperature ranges.

The hypothetical 2.6 mol/L concentration case predicted a sharp increase in MOST-system temperature, reaching approximately 235 °C, which also increased the final water outlet temperature. Although useful for identifying the sensitivity of device performance to MOST concentration, it should be interpreted only as an exploratory model outcome and not as a practical operating condition. Phase change effects, vapor pressure, and pressurization requirements were not included in the present model. This is particularly relevant for toluene, which has a relatively high vapor pressure and a boiling point of approximately 110 °C [44] at atmospheric pressure. Therefore, further assessment of solvent phase behavior, required pressure level, molecular and solvent stability, degradation, material compatibility, and safety constraints would be required before such concentrations or temperature ranges could be considered physically feasible for the present toluene-based system. Recent work [45] has also explored water/surfactant-based MOST systems to improve solvent safety compared with toluene.

The simulation results demonstrated the distinct performance of the two MOST systems. NBD1-QC1, representing long-term storage, required only 7% discharge in the activation component to reach the heat exchanger's inlet temperature. By the end of the system, the total discharge reached 31%. This gradual heat-release profile suggests its potential suitability for seasonal solar thermal energy storage and as a supplementary solution for progressive temperature boosting in existing heating systems. In contrast, NBD2-QC2, representing short-term storage, discharged 46% of its molecules in the activation component and reached full discharge upon entering the heat exchanger. This rapid heat-release profile is more suitable for immediate heat demands, such as peak shaving or local temperature boosting.

Scenario F showed that thermal enthalpy had a stronger influence on the activation-normalized discharge and water-heating ratios than the other individually varied parameters in the model. This suggests that the apparent activation barrier for QC-to-NBD back-conversion is an important device-design parameter for MOST-based co-heating applications. The result can guide future molecular development by indicating that activation-barrier control may be more influential for this application than increasing storage density alone. However, thermal enthalpy should not be interpreted as an independently adjustable molecular property. Molecular modifications that reduce the activation barrier may also affect storage half-life, energy density, absorption properties, cycling stability, and practical usability. Scenario F should therefore be viewed as a sensitivity analysis identifying an important design direction, for example through catalyst-assisted discharge or molecular design.

The results also highlight the importance of matching MOST properties and device operation to the intended application. For NBD1-QC1, lower concentrations improved activation-stage discharge performance but required longer activation lengths and reduced the achievable water outlet temperatures. Higher inlet temperatures of either water or MOST solution promoted further back-conversion in the heat exchanger. For NBD2-QC2, the shorter half-life and faster discharge behavior enabled stronger temperature-boosting performance, including at lower inlet water temperatures. These findings indicate that future device development should consider the combined effects of molecular properties, concentration, activation strategy, inlet temperatures, heat losses, compact geometry, and pressure drop.

A detailed cost analysis was outside the scope of this study, as MOST molecules are still under development and have not yet been scaled for domestic co-heating applications. The cost of a MOST-based device therefore cannot be reliably quantified at this stage, since it depends strongly on molecular synthesis routes and achievable production scale. Future work should include techno-economic comparison with established sensible and latent heat storage alternatives once scalable synthesis routes and MOST-device concepts are more mature.

6. Conclusion

This study investigated the discharge characteristics of molecular solar thermal storage (MOST) systems and evaluated their potential for water co-heating applications by combining experimental discharge characterization with numerical feasibility assessment of a conceptual co-heating device. Two norbornadiene-quadricyclane (NBD-QC) MOST systems with distinct half-lives were evaluated to represent long-term and short-term storage scenarios. Laboratory experiments assessed thermally triggered QC-to-NBD back-conversion for the first time, while numerical simulations examined the influence of molecular properties and device parameters on MOST discharge and activation-normalized water-heating performance.

The conclusions are as follows:

A. Experimental findings (Molecular properties)

- Back-conversion rates of QC to NBD molecules reached 95–100% at a MOST concentration of 1.3 mol/L (290.2 g/L), approaching the maximum reported in the literature [29]. This demonstrates successful thermally triggered back-conversion at relatively high concentration under the tested conditions.
- Higher activation temperatures reduced the residence time required for near-complete back conversion. At 90 °C, 95% conversion was achieved in 95 min, while 110 °C, 100% conversion was reached in 15 min. At a fixed temperature of 105 °C, increasing the residence time from 5 to 25 min improved conversion rates from 58% to 97%.

This confirmed that a residence time around five times the half-life enables near-complete conversion.
- The theoretical decay model used in numerical simulations was verified against experimental measurements. The model consistently provided conservative estimates of back conversion rates, with calculation errors ranging from 0% to 15%.

B. Simulation findings (*Co*-heating device)

- Numerical simulations demonstrated the conceptual feasibility of integrating MOST systems into a hot-water co-heating device under current molecular and device constraints, including the experimentally validated concentration of 1.3 mol/L. Since the simulations were conducted under idealized adiabatic assumptions, the activation-normalized water-heating ratios should be interpreted as upper-bound indicators for parameter comparison rather than as predicted practical device efficiencies.
- For the long-term MOST system NBD1-QC1 (half-life: 28 days at 25 °C), activation-normalized water-heating ratios ranged from 43% to 86%, assuming perfect insulation. Required discharge rates were 10–85%, corresponding to activation-normalized discharge ratios of 13–80%. This gradual discharge behavior indicates potential suitability for supplementary temperature boosting in systems where partial or progressive heat release is beneficial.
- For the short-term system NBD2-QC2 (half-life: 5 h at 25 °C), activation-normalized water-heating ratios ranged from 106% to 204% under the studied adiabatic scenarios. Complete discharge was generally required, yielding discharge efficiencies of 118–254%. Values above 100% reflect the recovery of stored chemical energy relative to the supplied activation heat. These characteristics support the use of NBD2-QC2 for rapid discharge applications such as peak shaving or temperature boosting.
- Among the parameters varied individually in the model, thermal enthalpy showed the strongest sensitivity effect on the activation-normalized discharge and water-heating ratios. A 10% reduction in thermal enthalpy substantially increased these ratios for both systems, indicating that activation-barrier control is an important consideration for future MOST development in co-heating applications.
- Device-specific design parameters, including MOST concentration and the operating temperatures of both MOST system and water, also strongly influenced performance. The results reveal a trade-off between activation-normalized water-heating ratios and outlet water temperature, highlighting the need to balance discharge behavior, target temperature, and application-specific operating conditions.

Future research should focus on molecular development and catalyst-assisted discharge strategies that improve activation-barrier control while maintaining storage stability, energy density, cycling durability, and practical usability. Experimental validation of the co-heating device, heat-loss reduction strategies, compact device geometries, and techno-economic comparison with established thermal storage alternatives are also needed to assess real-world applicability.

CRediT authorship contribution statement

Ali Naman Karim: Writing – review & editing, Writing – original draft, Visualization, Validation, Software, Methodology, Investigation, Formal analysis, Data curation, Conceptualization. **Giovana Fantin Do Amaral Silva:** Software, Conceptualization. **Zakariaa Refaa:** Writing – review & editing, Software, Investigation, Data curation, Conceptualization. **Zhihang Wang:** Writing – review & editing, Visualization, Investigation, Conceptualization. **Jessica Orrego Hernandez:** Investigation, Conceptualization. **Liang Fei:** Investigation. **Pär Johansson:** Writing – review & editing, Supervision, Project administration, Funding acquisition, Conceptualization. **Angela Sasic Kalagasidis:** Writing – review & editing, Supervision, Project administration, Funding acquisition, Conceptualization. **Kasper Moth-Poulsen:** Writing – review & editing, Supervision, Resources, Project administration, Funding acquisition, Conceptualization.

Declaration of competing interest

The authors declare that they have no known competing financial interests or personal relationships that could have appeared to influence the work reported in this paper.

Acknowledgments

The financial support from Chalmers Areas of Advance Energy, Department of Architecture and Civil Engineering, Chalmers University of Technology, Swedish Energy Agency, Swedish Research council, and European Union's Horizon 2020 Framework Programme under grant agreement no. 951801 is gratefully acknowledged.

Appendix A. Pipe dimension and spatial resolution

A preliminary study was conducted to determine the minimum required inner pipe radius containing MOST system (r_1) and the spatial resolution (dx) in the numerical simulation model. The objective was to minimize calculation errors while ensuring optimal water outlet temperatures.

Pipe dimension:

The inner pipe radius (r_1) was selected to ensure a minimum water outlet temperature of 60 °C under the base-line scenario defined in this paper. To adopt a conservative approach, the MOST system inlet temperature in the heat exchanger ($T_{M.0}$) was reduced from 105 °C to 80 °C. This adjustment ensured that the outlet temperature of 60 °C could be reached even under suboptimal conditions. As shown in Fig. A1a, achieving this target required an r_1 greater than 3 mm. Consequently, a pipe radius of 3.5 mm was selected for parametric study.

Spatial resolution:

The calculation error in the activation component $Error_{act}$ (%) was defined as the percentage discrepancy between the theoretical heat required $Q_{M.max}$ (W) and the sum of the numerically calculated activation heat $Q_{M.act}$ (W) and the discharge heat $Q_{M.rel}$ (W). This relationship is expressed in Eq. A.1:

$$Error_{act} = 100 \bullet \left| \frac{Q_{M.max} - (Q_{M.act} + Q_{M.rel})}{Q_{M.max}} \right| \quad (A.1)$$

Similarly, the calculation error in the heat exchanger $Error_{hex}$ (%) was defined as the percentage discrepancy between the theoretical heat required to raise the water temperature $Q_{w.hex}$ (W) and the sum of the heat transferred from the MOST system to the water $Q_{M.hex}$ (W) and the discharge heat within the heat exchanger $Q_{M.rel.hex}$ (W). This is expressed in Eq. (A.2):

$$Error_{hex} = 100 \bullet \left| \frac{Q_{w.hex} - (Q_{M.hex} + Q_{M.rel.hex})}{Q_{w.hex}} \right| \quad (A.2)$$

Based on the results (Fig. A1b), a spatial step (dx) of 0.7 mm was selected to balance accuracy and computational efficiency. This resolution produced errors of approximately 0.005% in the activation component and 0.21% in the heat exchanger, which were considered sufficiently accurate for this study. For the chosen flow velocity of 0.007 m/s, the selected spatial step corresponds to a time step of 0.1 s. This was calculated to accommodate a total simulation duration of 3600 s across a total pipe length of approximately 25 m.

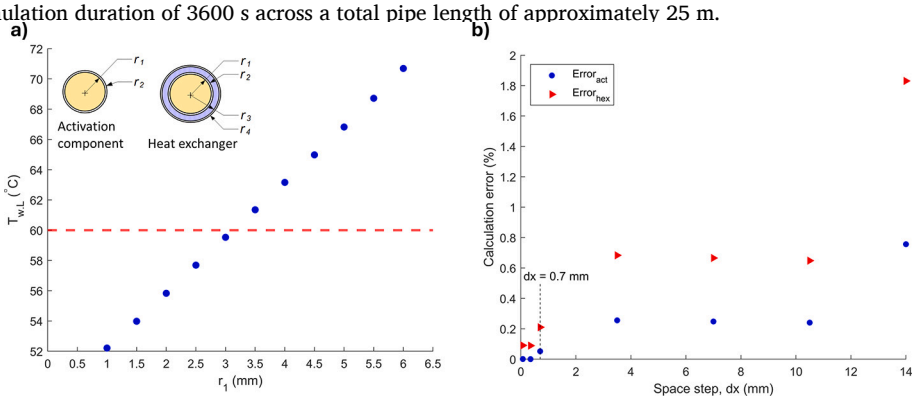

Fig. A1. a) Calculated water outlet temperature in the device as a function of the inner pipe radius containing MOST systems. b) Calculation errors in the activation component and heat exchanger of the numerical thermal model as a function of the selected spatial step.

Appendix B. Numerical simulation results

Appendix B compiles detailed results from the parametric study conducted using numerical simulations. The scenarios (A-F) for both NBD1-QC1 and NBD2-QC2 MOST systems are presented in Figs. B1 to B12. Each figure includes the following four plots (a-d):

- a) Temperature profile of the MOST system.
- b) Water temperature in the device.
- c) Discharge rate, β.
- d) Activation-normalized MOST discharge and water-heating ratios for each scenario.

Some scenarios, particularly the high-concentration sensitivity cases, may predict temperatures outside the experimentally validated operating range; these results should therefore be interpreted as exploratory model outcomes rather than practical operating conditions.

B.1. Scenario 1-A & 2-A: t_{act}

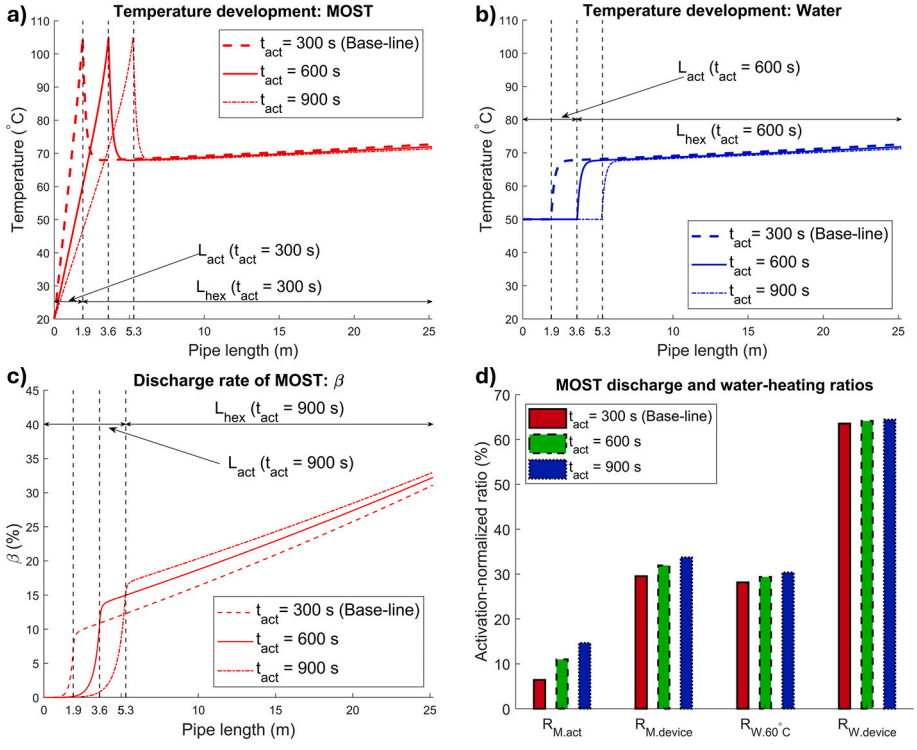

Fig. B1. Scenario 1-A. Impact of activation rate: NBD1-QC1.

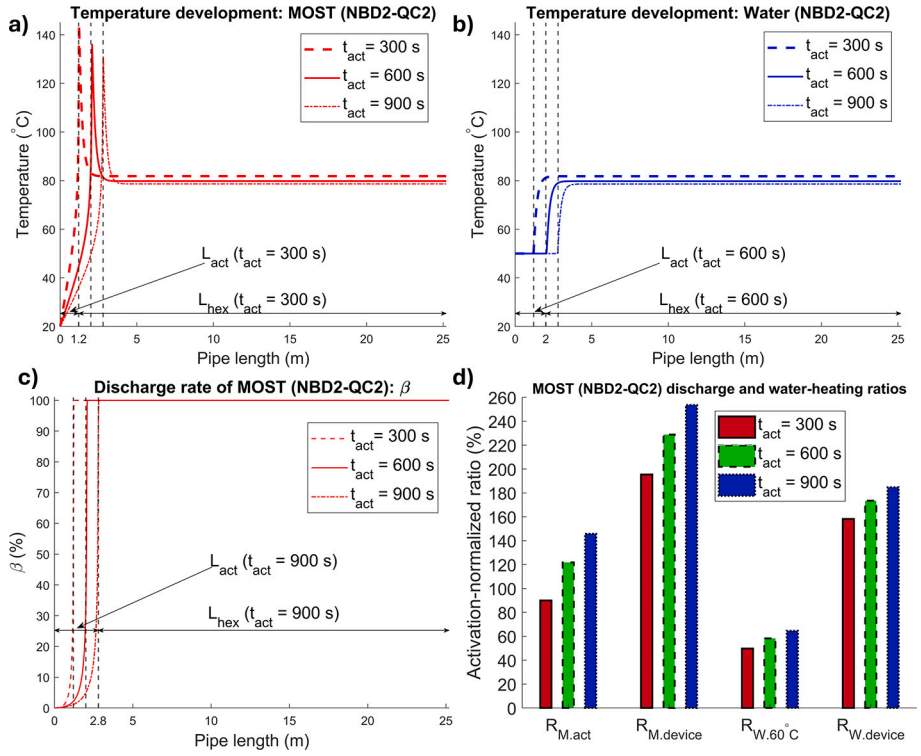

Fig. B2. Scenario 2-A. Impact of activation rate: NBD2-QC2.

B.2. Scenario 1-B & 2-B: $T_{M.0}$

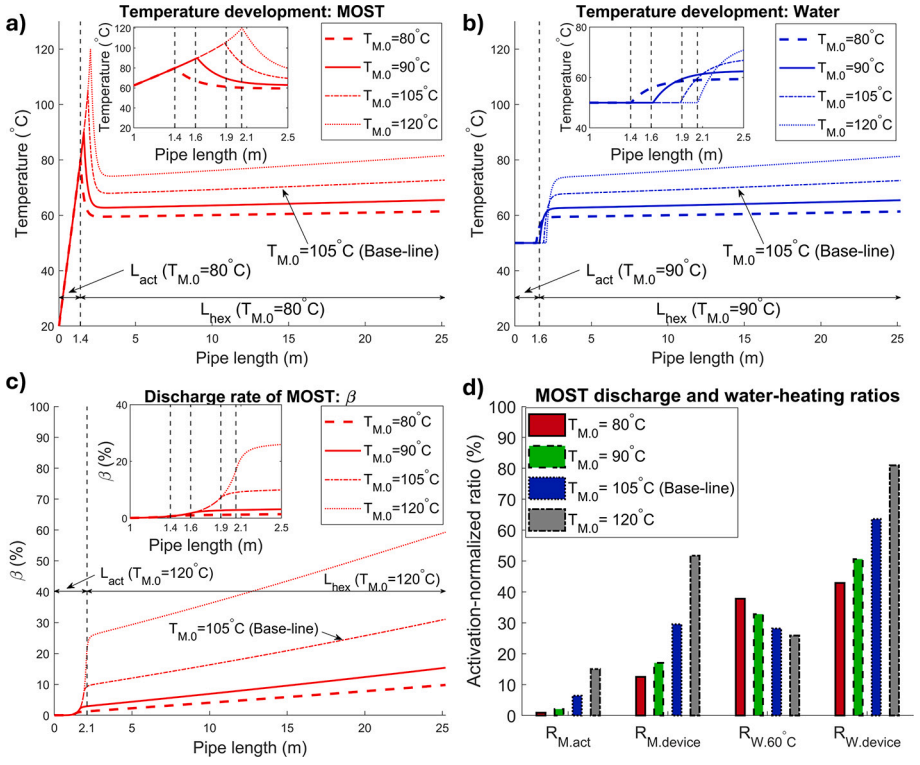

Fig. B3. Scenario 1-B. Impact of MOST system inlet temperature in the heat exchanger: NBD1-QC1.

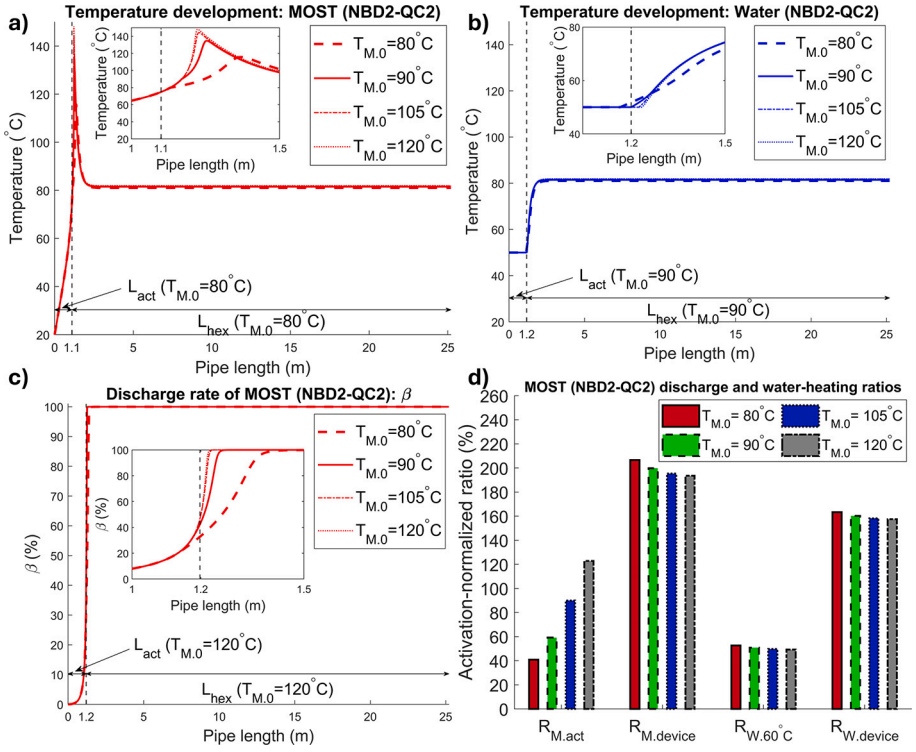

Fig. B4. Scenario 2-B. Impact of MOST system inlet temperature in the heat exchanger: NBD2-QC2.

B.3. Scenario 1-C: $T_{W.0}$

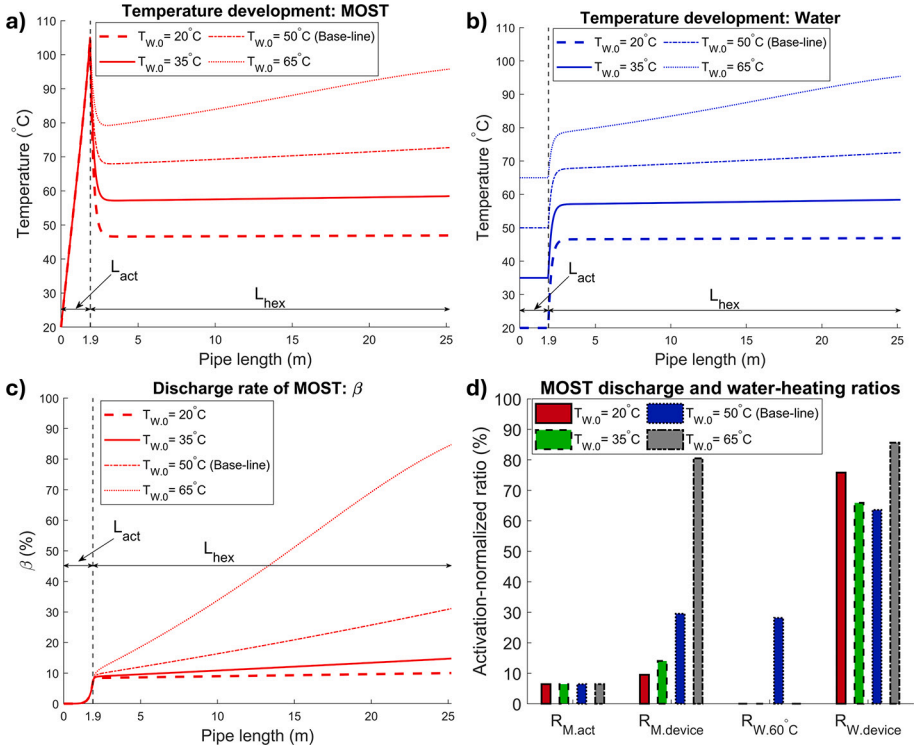

Fig. B5. Scenario 1-C. Influence of water inlet temperature in the heat exchanger: NBD1-QC1.

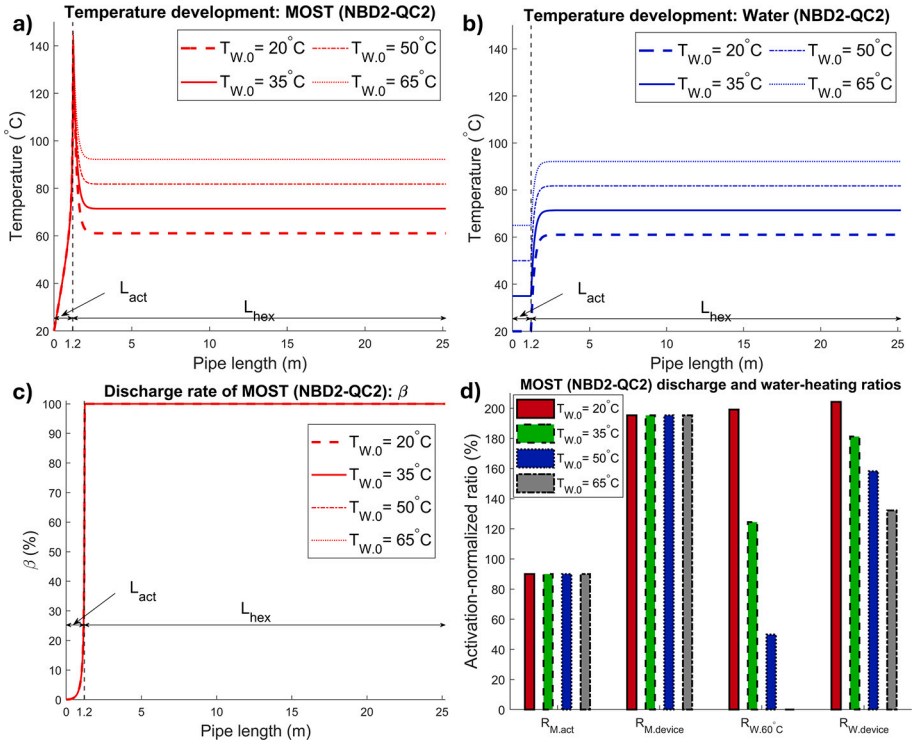

Fig. B6. Scenario 2-C. Influence of water inlet temperature in the heat exchanger: NBD2-QC2.

B.4. Scenario 1-D: A_{00}

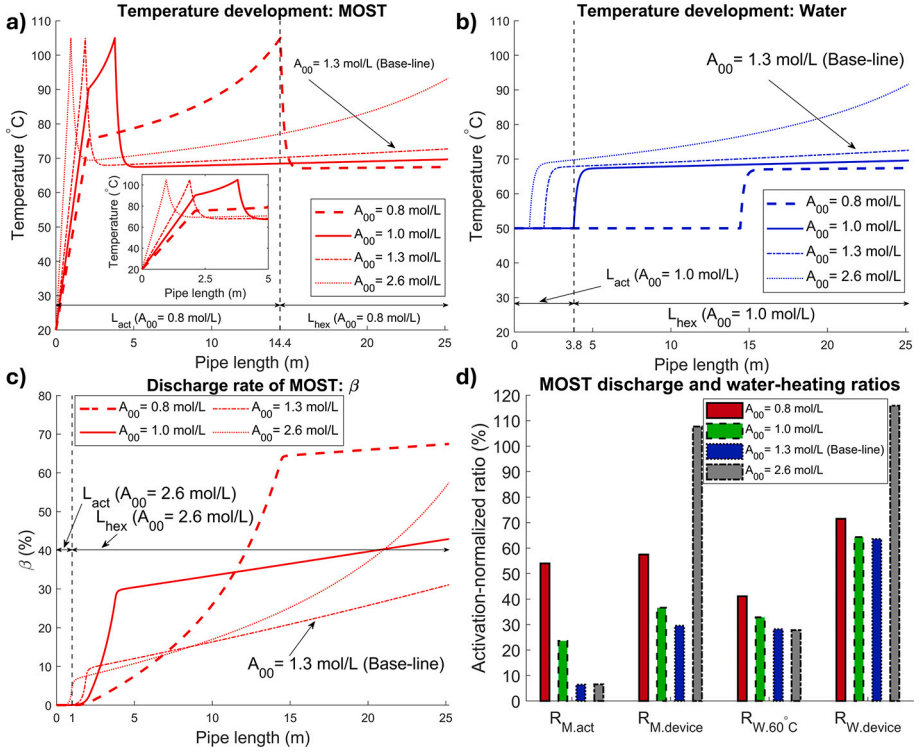

Fig. B7. Scenario 1-D. Impact of initial molecular concentration of MOST system: NBD1-QC1.

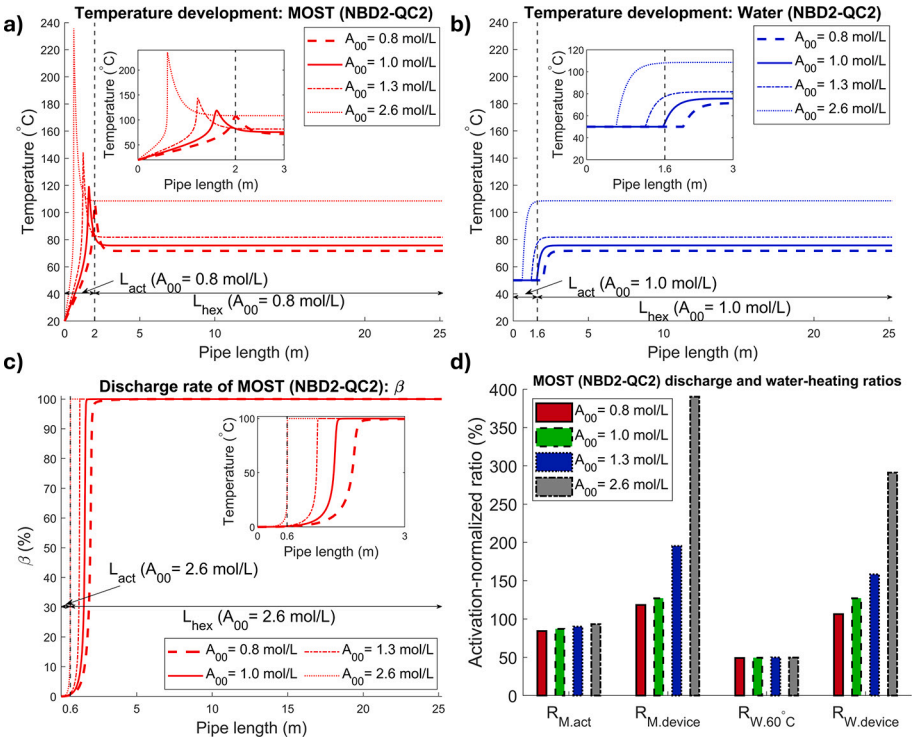

Fig. B8. Scenario 2-D. Impact of initial molecular concentration of MOST system: NBD2-QC2.

B.5. Scenario 1-E: $\Delta H_{storage}$

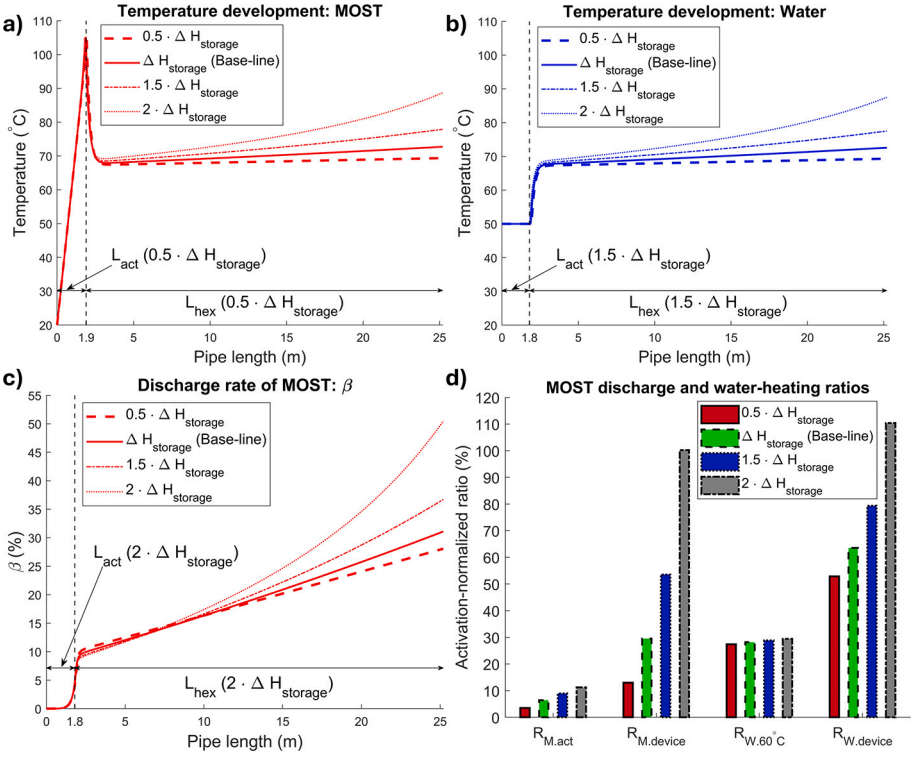

Fig. B9. Scenario 1-E. Impact of thermal energy storage capacity of MOST system: NBD1-QC1.

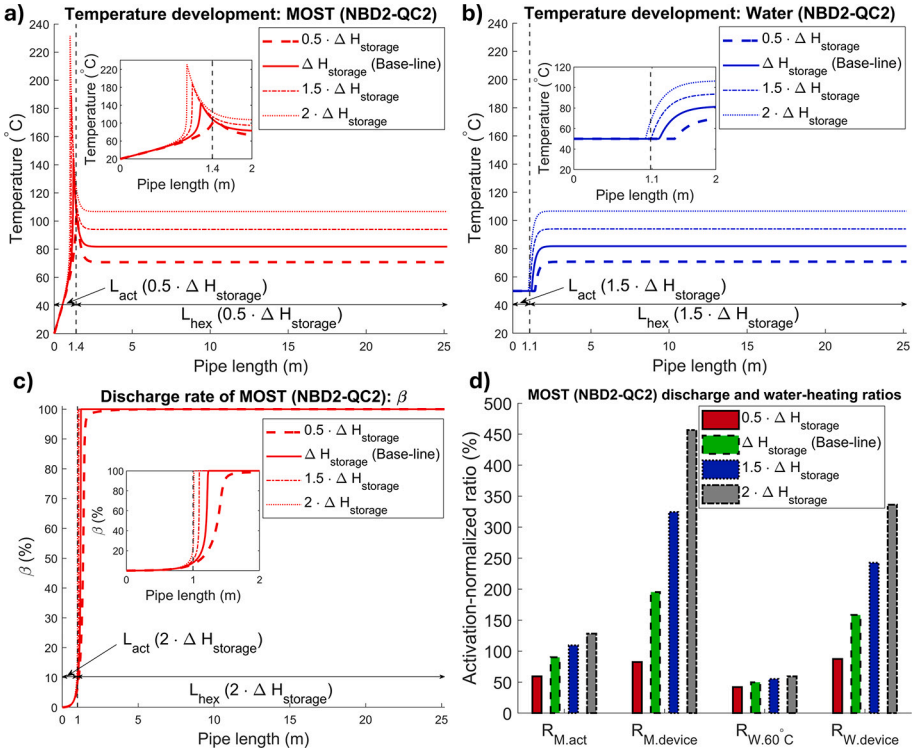

Fig. B10. Scenario 2-E. Impact of thermal energy storage capacity of MOST system: NBD2-QC2.

B.6. Scenario 1-F & 2-F: $\Delta H_{thermal}$

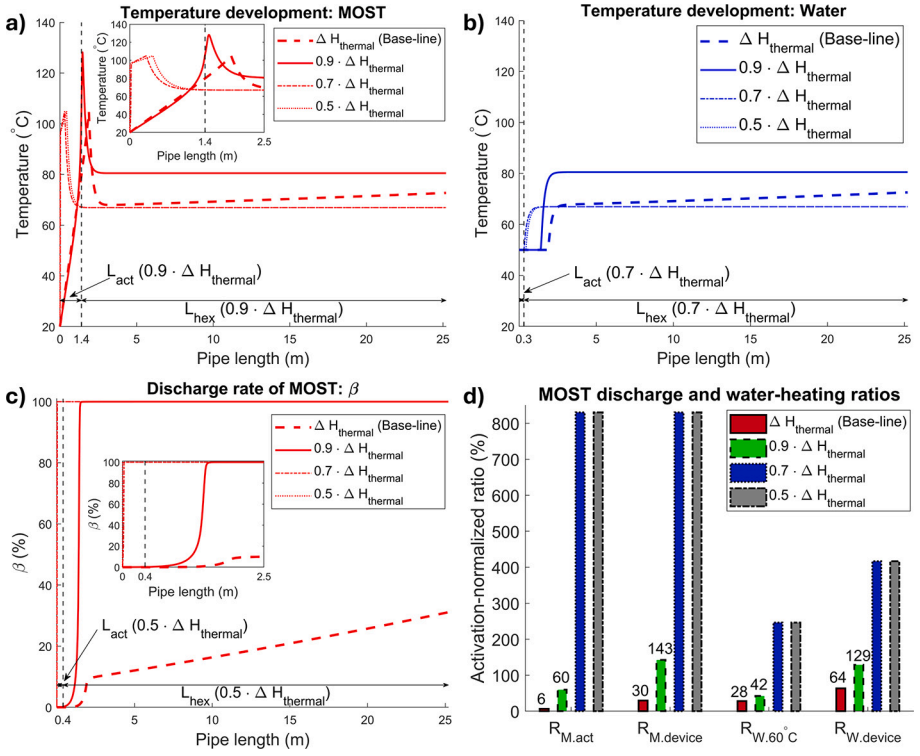

Fig. B11. Scenario 1-F. Impact of thermal enthalpy of MOST system: NBD1-QC1.

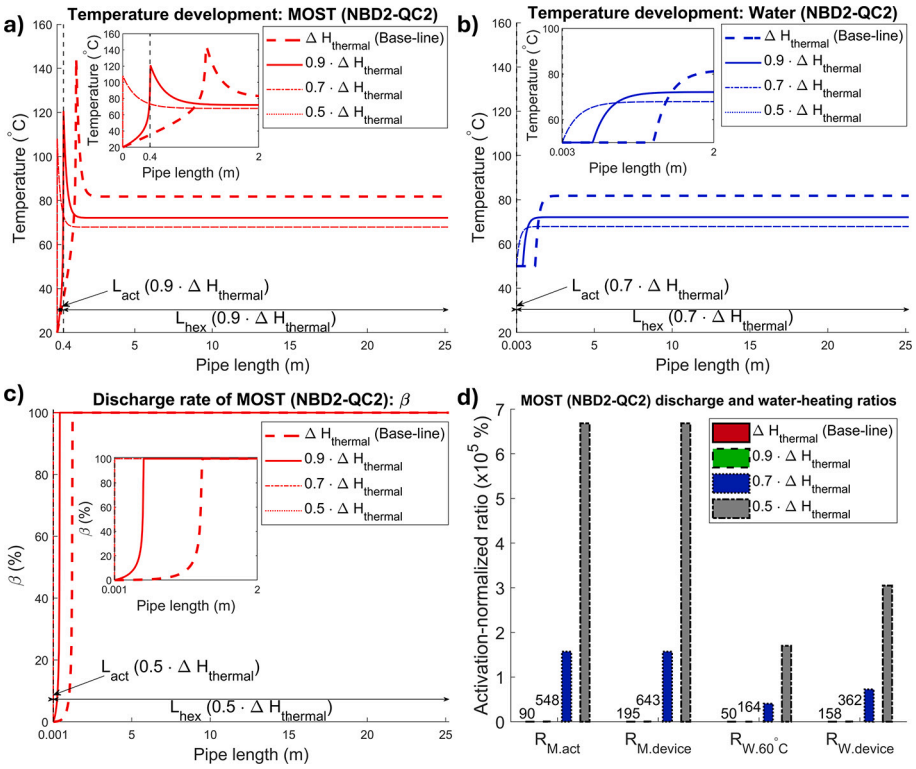

Fig. B12. Scenario 2-F. Impact of thermal enthalpy of MOST system: NBD2-QC2.

Appendix C. Heat loss

Appendix C presents a case study analyzing the impact of heat losses in the heat exchanger on the temperature development for the base-line scenario with both MOST systems (Fig. 12). As described in Section 3.2.2, adiabatic boundaries were considered for the pipes both in the activation component and the heat exchanger. To evaluate the influence of heat losses, the original heat balance equation (Eq. 24) was further developed into Eq. (C.1), supported by Eq. (C.2) and (C.3).

$$v_M \frac{\partial T_M}{\partial x} - v_w \frac{\partial T_w}{\partial x} = \frac{q_{rel}(x) + q_{hex.M}(x)}{\rho_M \bullet c_{p.M}} - \frac{q_{hex.w}(x)}{\rho_w \bullet c_{p.w}} - \frac{q_{loss.w}(x)}{\rho_w \bullet c_{p.w}} \tag{C.1}$$

$$q_{loss.w}(x) = \frac{Q_{loss}(x)}{V_w(x)} \tag{C.2}$$

$$Q_{loss}(x) = \frac{dx \bullet (T_w(x) - T_{amb})}{\frac{\ln\left(\frac{r_4}{r_3}\right)}{2\pi \bullet \lambda_{pipe}} + \frac{\ln\left(\frac{r_{ins}}{r_4}\right)}{2\pi \bullet \lambda_{ins}} + \frac{1}{2\pi \bullet r_{ins} \bullet (\alpha_{convection} + \alpha_{radiation})}} \tag{C.3}$$

Where $q_{loss.W}(W/m^3)$ is the volumetric heat loss to the surroundings, Q_{loss} (W) is the heat loss from the discretized pipe segment, r_{ins}(m) is the exterior radius of the insulation layer, T_{amb} (°C) is ambient air temperature. The radii r_3 and r_4 (m) are defined according to Fig. 8, where r_3 is the inner radius of the outer pipe wall and r_4 is the outer radius of the outer pipe wall. λ_{pipe} and λ_{ins} (W/(m•K)) are the thermal conductivities of the pipe wall and insulation material, respectively. $\alpha_{convection}, \alpha_{radiation}$ (W/(m^2•K)) are the external convective and radiative heat transfer coefficients, respectively.

All design parameters were consistent with the base-line scenario (Table 2), with the ambient temperature T_{amb} set to 20 °C. The pipes were assumed to be insulated with a 15-mm thick layer of insulation ($\lambda_{insulation}$ =0.036 W/(m•K)). For simplicity, it was assumed that the exterior of the insulation was covered with an ultra-low-emissivity layer, allowing for negligible radiative heat transfer at the surface. A parametric study was conducted to assess the impact of $\alpha_{convection}$ on heat losses and temperature development, considering values ranging from 0 to 6 W/(m^2•K). A value of 6 W/(m^2•K) represents relatively high air velocities parallel to the exterior pipe surfaces, simulating forced convection or outdoor conditions. Conversely, a value of 0 W/(m^2•K), represents natural convection ($\alpha_{convection} = 2 \bullet |T_{amb} - T_s|^{0.25}$ [34]) with no temperature difference between the exterior pipe surface (T_s (°C)) and the ambient air. At a temperature difference of approximately 0.06 °C and 1 °C, $\alpha_{convection}$ equals 1 and 2 W/(m^2•K), respectively.

It should be noted that the simulated ~ 25 m heat-exchanger length represents a conservative straight-pipe configuration with direct exposure to the prescribed ambient condition along the full length. For the studied configuration, the characteristic thermal length was approximately 5 m, meaning that over a 25 m pipe length the remaining temperature difference relative to the initial value is less than 1%, as approximated by e^{-L/L_c} [34]. This explains why the heat-loss effect becomes particularly pronounced towards the outlet in the straight-pipe simulation. In practical heat-exchanger

design, however, the pipe arrangement may be compacted into multiple adjacent passes, where neighboring high-temperature pipes reduce the effective temperature difference to the surroundings. Therefore, the magnitude of the heat-loss effect observed towards the end of the 25 m pipe should be interpreted as strongly dependent on the selected technical design and pipe arrangement. Nevertheless, the results remain useful for illustrating the sensitivity of the system to non-adiabatic boundary conditions.

The results (Fig. C1) revealed that at $\alpha_{convection}$=0 W/(m^2•K), temperature deviations remained below 0.5 °C closely matching the adiabatic baseline (Fig. 12). However, at $\alpha_{convection}$=1 W/(m^2•K), significant performance degradation was observed, highlighting the critical need to minimize convective heat losses. Notably, despite the conservative straight-pipe heat-loss assumption, a water outlet temperature of 60 °C was still achievable for both MOST systems under the tested conditions.

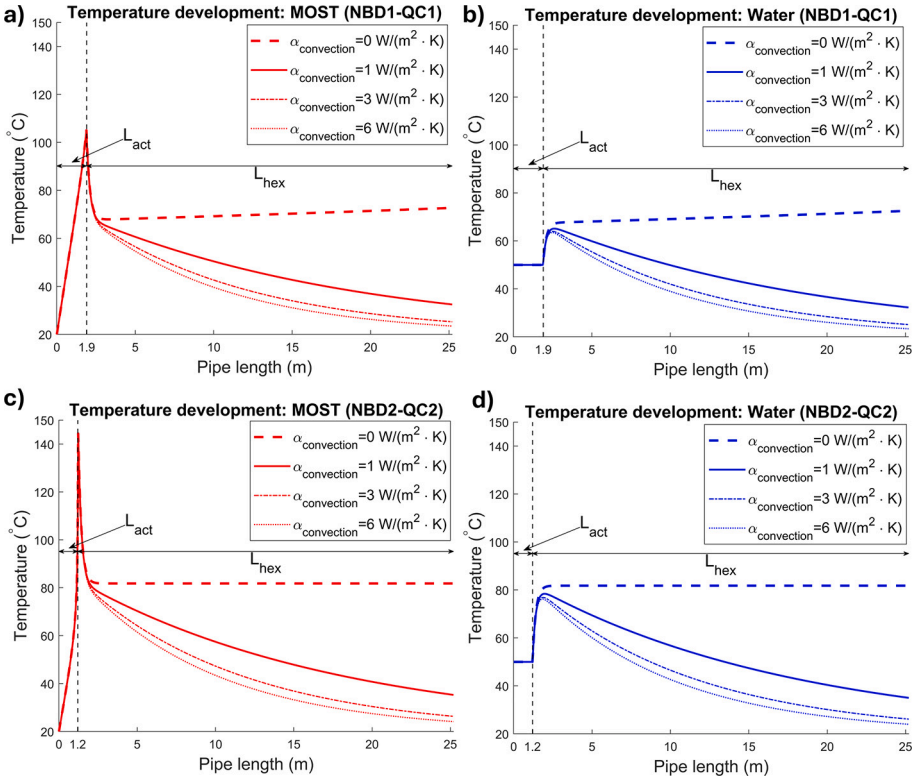

Fig. C1. Case study on the impact of heat losses to the surroundings on the temperature development in the heat exchanger for variable convective heat transfer coefficients: a,b) NBD1-QC1, c,d) NBD2-QC2.

Appendix D. Replicate back-conversion measurements

To assess reproducibility of the NMR-based conversion results, two additional replicate measurements were performed for QC1-to-NBD1 back-conversion at 105 °C and 25 min residence time (Fig. D1), following the same testing procedure outlined in Section 2.2.2. This condition was selected because it represents near-complete conversion in the residence-time study. Together with the original measurement (Fig. 11a), the replicate measurements confirmed reproducible near-complete back-conversion, with conversion rates ranging from 97% to 98% under the tested condition.

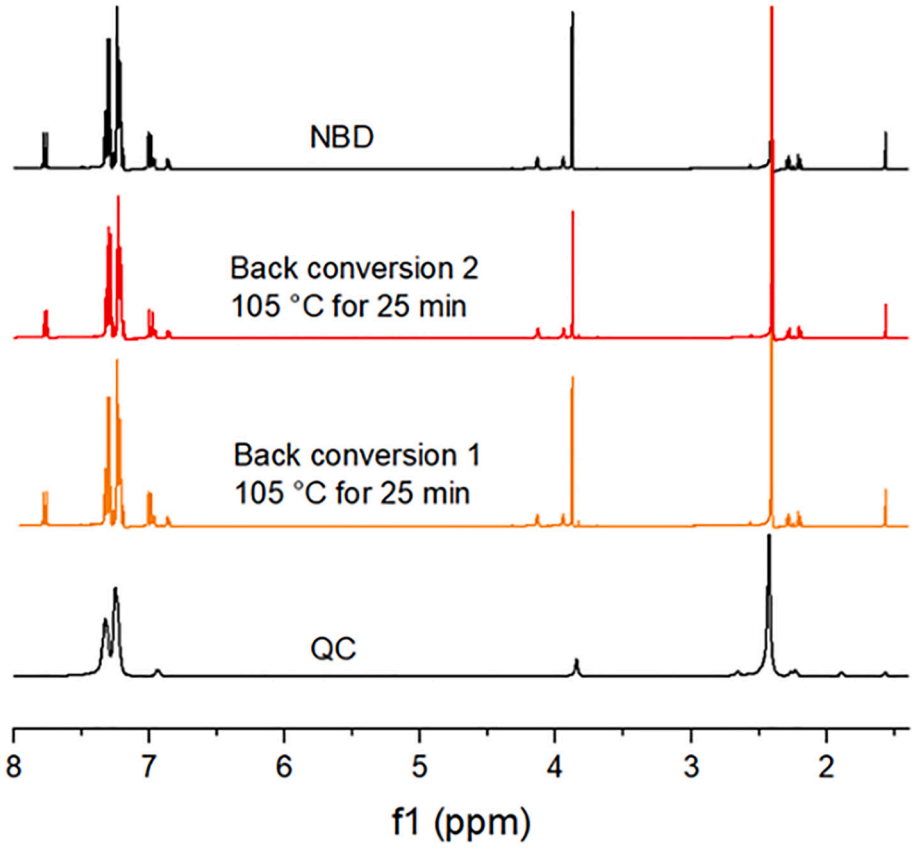

Fig. D1. Replicate ^{1}H NMR spectra (400 MHz, toluene-d_8) for QC1-to-NBD1 back-conversion at 105 °C and 25 min residence time.

Data availability

Data will be made available on request.

References

[1] European Commission, Renewable Energy Targets. https://energy.ec.europa.eu/topics/renewable-energy/renewable-energy-directive-targets-and-rules/renewable-energy-targets_en, 2023. (Accessed 9 January 2026).

[2] Eurostat, Eurostat's Latest Data Reveals a Growth on the Share of Renewables in Heating and Cooling!. https://www.euroheat.org/news/eurostat-s-latest-data-reveals-a-growth-on-the-share-of-renewables-in-heating-and-cooling-1, 2025.

[3] I. Sarbu, C. Sebarchievici, A comprehensive review of thermal energy storage, Sustainability 10 (2018), https://doi.org/10.3390/su10010191.

[4] O.S. Miljanic, J.A. Pratt, Introduction to Energy and Sustainability, John Wiley & Sons, 2021.

[5] Z. Wang, H. Hölzel, K. Moth-Poulsen, Status and challenges for molecular solar thermal energy storage system based devices, Chem. Soc. Rev. 51 (2022) 7313–7326, https://doi.org/10.1039/d1cs00890k.

[6] M. Quant, A. Lennartson, A. Dreos, M. Kuisma, P. Erhart, K. Börjesson, et al., Low molecular weight norbornadiene derivatives for molecular solar-thermal energy storage, Chem. - A Eur. J. 22 (2016) 13265–13274, https://doi.org/10.1002/chem.201602530.

[7] A. Dreos, K. Börjesson, Z. Wang, A. Roffey, Z. Norwood, D. Kushnir, et al., Exploring the potential of a hybrid device combining solar water heating and molecular solar thermal energy storage, Energy Environ. Sci. 10 (2017) 728–734, https://doi.org/10.1039/c6ee01952h.

[8] M. Mansø, A.U. Petersen, Z. Wang, P. Erhart, M.B. Nielsen, K. Moth-Poulsen, Molecular solar thermal energy storage in photoswitch oligomers increases energy densities and storage times, Nat. Commun. 9 (2018) 1–7, https://doi.org/10.1038/s41467-018-04230-8.

[9] Z. Refaa, A. Hofmann, M.F. Castro, J.O. Hernandez, Z. Wang, H. Hölzel, et al., Thermo-optical performance of molecular solar thermal energy storage films, Appl. Energy 310 (2022), https://doi.org/10.1016/j.apenergy.2022.118541.

[10] R. Schulte, S. Afflerbach, T. Paululat, H. Ihmels, Bis- and tris-norbornadienes with high energy densities for efficient molecular solar thermal energy storage, Angew. Chem. 135 (2023), https://doi.org/10.1002/ange.202309544.

[11] Z. Wang, H. Hölzel, L. Fernandez, A.S. Aslam, P. Baronas, J. Orrego-Hernández, et al., Hybrid solar energy device for simultaneous electric power generation and molecular solar thermal energy storage, Joule (2024) 1–16, https://doi.org/10.1016/j.joule.2024.06.012.

[12] A. Lennartson, K. Moth-Poulsen, Molecular solar-thermal energy storage: molecular design and functional devices, in: Haining Tian, A.H. Gerrit Boschloo (Eds.), Mol. Devices Sol. Energy Convers. Storage, 2018, pp. 327–352, https://doi.org/10.1007/978-981-10-5924-7_9.

[13] K. Moth-Poulsen, D. Ćoso, K. Börjesson, N. Vinokurov, S.K. Meier, A. Majumdar, et al., Molecular solar thermal (MOST) energy storage and release system, Energy Environ. Sci. 5 (2012) 8534–8537, https://doi.org/10.1039/C2EE22426G.

[14] W. Feng, W. Luo, Y. Feng, Photo-responsive carbon nanomaterials functionalized by azobenzene moieties: structures, properties and application, Nanoscale 4 (2012) 6118–6134, https://doi.org/10.1039/C2NR31505J.

[15] M. Brøndsted Nielsen, N. Ree, K.V. Mikkelsen, M. Cacciarini, Tuning the dihydroazulene – vinylheptafulvene couple for storage of solar energy, Russ. Chem. Rev. 89 (2020) 573–586, https://doi.org/10.1070/RCR4944.

[16] J. Fang, H. Wu, T. Liu, Z. Zheng, J. Lei, Q. Liu, et al., Thermodynamic evaluation of a concentrated photochemical–photovoltaic–thermochemical (CP-PV-T) system in the full-spectrum solar energy utilization, Appl. Energy 279 (2020) 115778, https://doi.org/10.1016/j.apenergy.2020.115778.

[17] J. Fang, Q. Liu, S. Guo, J. Lei, H. Jin, Spanning solar spectrum: a combined photochemical and thermochemical process for solar energy storage, Appl. Energy 247 (2019) 116–126, https://doi.org/10.1016/j.apenergy.2019.04.043.

[18] H.P.Q. Nguyen, A.J. Maertens, B.A. Baker, M. Nathan, W. Wu, Z. Ye, et al., Molecular solar thermal energy storage in Dewar pyrimidone beyond 1, in: 6 Megajoules Per Kilogram Molecular Solar Thermal Energy Storage in Dewar Pyrimidone Beyond 1. 6 Megajoules Per Kilogram, 2026, https://doi.org/10.1126/science.aec6413.

[19] Harald Mehling LFC, Heat and cold storage with PCM vol. 3, Speinger, 2008.

[20] M.H. Hansen, S.T. Olsen, K.O. Sylvester-Hvid, K.V. Mikkelsen, Simulation framework for screening of molecular solar thermal systems in the context of a hybrid device, Chem. Phys. 519 (2019) 92–100, https://doi.org/10.1016/j.chemphys.2018.10.020.

[21] A.D. Dubonosov, A. Bren, V.A. Chernoivanov, Norbornadiene–quadricyclane as an abiotic system for the storage of solar energy, Russ. Chem. Rev. 71 (2002) 917–927, https://doi.org/10.1070/RC2002v071n11ABEH000745.

[22] N. Baggi, L.M. Muhammad, Z. Liasi, J.L. Elholm, P. Baronas, E. Molins, et al., Exploring ortho-dianthrylbenzenes for molecular solar thermal energy storage, J. Mater. Chem. A 12 (2024), https://doi.org/10.1039/d4ta03879g.
[23] M. Jevric, A.U. Petersen, M. Mansø, S. Kumar Singh, Z. Wang, A. Dreos, et al., Norbornadiene-based photoswitches with exceptional combination of solar spectrum match and long-term energy storage, Chemistry (Weinheim an der Bergstrasse, Germany) 24 (2018) 12767–12772, https://doi.org/10.1002/chem.201802932.
[24] Z. Wang, H. Moïse, M. Cacciarini, M.B. Nielsen, M. aki Morikawa, N. Kimizuka, et al., Liquid-based multijunction molecular solar thermal energy collection device, Adv. Sci. 8 (2021) 1–6, https://doi.org/10.1002/advs.202103060.
[25] Z. Wang, Z. Wu, Z. Hu, J. Orrego-Hernández, E. Mu, Z.Y. Zhang, et al., Chip-scale solar thermal electrical power generation, Cell Rep. Phys. Sci. 3 (2022), https://doi.org/10.1016/j.xcrp.2022.100789.
[26] G.G.D. Han, H. Li, J.C. Grossman, Optically-controlled long-term storage and release of thermal energy in phase-change materials, Nat. Commun. 8 (2017), https://doi.org/10.1038/s41467-017-01608-y.
[27] G.G.D. Han, J.H. Deru, E.N. Cho, J.C. Grossman, Optically-regulated thermal energy storage in diverse organic phase-change materials, Chem. Commun. 54 (2018) 10722–10725, https://doi.org/10.1039/C8CC05919E.
[28] Y. Shi, M.A. Gerkman, Q. Qiu, S. Zhang, G.G.D. Han, Sunlight-activated phase change materials for controlled heat storage and triggered release, J. Mater. Chem. A 9 (2021) 9798–9808, https://doi.org/10.1039/D1TA01007G.
[29] Z. Wang, A. Roffey, R. Losantos, A. Lennartson, M. Jevric, A.U. Petersen, et al., Macroscopic heat release in a molecular solar thermal energy storage system, Energy Environ. Sci. 12 (2019) 187–193, https://doi.org/10.1039/c8ee01011k.
[30] Z. Wang, Molecular Solar Thermal Energy Storage System: Evaluation of Different Candidates- Characterization, Modification and Integration of Different Candidates, . CHALMERS UNIVERSITY OF TECHNOLOGY,, 2019.
[31] K.J. Laidler, M.C. King, Development of transition-state theory, J. Phys. Chem. 87 (1983) 2657–2664, https://doi.org/10.1021/j100238a002.
[32] H. Eyring, The activated complex in chemical reactions, J. Chem. Phys. 3 (1935) 107–115.
[33] Z. Wang, J. Udmark, K. Börjesson, R. Rodrigues, A. Roffey, M. Abrahamsson, et al., Evaluating dihydroazulene/vinylheptafulvene photoswitches for solar energy storage applications, ChemSusChem 10 (2017) 3049–3055, https://doi.org/10.1002/cssc.201700679.
[34] C.E. Hagentoft, Introduction to Building Physics, Student litteratur, 2001.
[35] V.M. Shulga, F.G. Eldarov, Y.A. Atanov, A.A. Kuyumchev, Thermal conductivity and heat capacity of liquid toluene at temperatures between 255 and 400 K and at pressures up to 1000 MPa, Int. J. Thermophys. 7 (1986) 1147–1161, https://doi.org/10.1007/BF00503972.
[36] T.F. Sun, S.A.R.C. Bominaar, C.A. Ten Seldam, S.N. Biswas, Evaluation of the thermophysical properties of toluene and n-heptane from 180 to 320 K and up to 260 MPa from speed-of-sound data, Ber. Bunsenges. Phys. Chem. 95 (1991) 696–704, https://doi.org/10.1002/bbpc.19910950607.
[37] E.J. Wucherer, A. Wilson, Chemical, Physical and Hazards Properties of Quadricyclane. California, 1998.
[38] K. Stranius, K. Börjesson, Determining the photoisomerization quantum yield of photoswitchable molecules in solution and in the solid state, Sci. Rep. 7 (2017) 1–9, https://doi.org/10.1038/srep41145.
[39] T.L. Bergman, Fundamentals of heat and mass transfer, John Wiley & Sons, 2011.
[40] A. Bejan, A.D. Kraus, Heat transfer handbook vol. 1, John Wiley & Sons, 2003.
[41] S. Kakaç, A. Pramuanjaroenkij, Review of convective heat transfer enhancement with nanofluids, Int. J. Heat Mass Transf. 52 (2009) 3187–3196, https://doi.org/10.1016/j.ijheatmasstransfer.2009.02.006.
[42] Daniel Olsson, Tappvarmvatten i flerbostadshus [Domestic Hot Water in Multi-dwelling Buildings], Rapport 2003:4 (In Swedish), 2003.
[43] Energimyndighet, Mätning av kall- och varmvattenanvändning i 44 hushåll [Measurement of cold and hot water use in 44 households] (In Swedish), 2009.
[44] National Institute of Standards and Technology, Toluene. NIST Chem WebBook, NIST Stand Ref Database Number 69. https://webbook.nist.gov/cgi/cbook.cgi?ID=C108883, 1998 (accessed May 16, 2026).
[45] L. Fernandez, H. Hölzel, P. Ferreira, N. Baggi, K. Moreno, Z. Wang, et al., Surfactant-enabled strategy for molecular solar thermal energy storage systems in water, Green Chem. 27 (2025) 14119–14130, https://doi.org/10.1039/d5gc04357c.